ARTICLE IN PRESS



Available online at www.sciencedirect.com

ScienceDirect

Geochimica et Cosmochimica Acta xxx (2021) xxx-xxx

Geochimica et Cosmochimica Acta

www.elsevier.com/locate/gca

A reactive transport approach to modeling cave seepage water chemistry I: Carbon isotope transformations

Jennifer L. Druhan ^{a,*}, Corey R. Lawrence ^b, Aaron K. Covey ^c, Max G. Giannetta ^a, Jessica L. Oster ^c

^a Department of Geology, University of Illinois, Urbana-Champaign, IL, United States
^b U. S. Geological Survey, Denver, CO, United States
^c Department of Earth and Environmental Sciences, Vanderbilt University, Nashville, TN, United States

Received 8 December 2020; accepted in revised form 30 June 2021; available online xxxx

Abstract

The majority of Critical Zone research has emphasized silicate lithologies, which are typified by relatively slow rates of reactivity and incongruent weathering. However, the relatively simpler weathering of carbonate-dominated lithology can result in secondary mineral deposits, such as speleothems, which provide a long-term archive for Critical Zone processes. In particular, carbon isotopic variability in speleothems has the potential to provide records of changes in vegetation, soil respiration, carbon stabilization in deep soils, and/or chemical weathering in the host rock. Despite this opportunity to reconstruct many Critical Zone processes, multiple influences can also make interpretion of these speleothem carbon isotope records challenging. The integration of observational data and simulations specific to karst systems offers an interpretive framework for these unique time-averaged records accumulated through the evolution of carbonate landscapes. Here, we present a forward and process-based reactive transport simulation based on a multi-year monitoring study of Blue Spring Cave in central Tennessee, USA. The simulations describe the fluid-driven weathering of limestone including explicit tracking of dissolved calcium, stable carbon, and radiocarbon isotope ratios based on reaction rates calibrated through laboratory batch reaction data. We find that calcium concentrations and radiocarbon isotope ratios are strongly influenced by the combination of fluid flow rate and soil CO₂ content, and require rapid gas phase communication between the overlying soil boundary condition and interior karst to sustain both elevated limestone weathering rates and relatively modern radiocarbon signatures. Stable carbon isotopes are largely dictated by temperature-dependent equilibrium fractionation among contemporaneous species. These simulations are extended to a wide range of parameter space to demonstrate the environmental factors that these isotope proxies record.

© 2021 Elsevier Ltd. All rights reserved.

Keywords: Cave drip water chemistry; Carbon isotopes; Reactive transport modeling

1. INTRODUCTION

Carbonate-dominated Critical Zones are unique in that they frequently host caves which provide access to subsurface waters. The chemistry of these fluids record water-

* Corresponding author.

E-mail address: jdruhan@illinois.edu (J.L. Druhan).

https://doi.org/10.1016/j.gca.2021.06.041

0016-7037/© 2021 Elsevier Ltd. All rights reserved.

soil-rock interactions across multiple length and timescales. Through the sampling of waters from soils and drip sites within a cave over multiple years, we can observe how seasonal and interannual changes in temperature and infiltration are recorded in the chemical signatures of seepage waters and how these signals are modified along flow paths (Oster et al., 2012; Wong et al., 2015). The subsurface voids opened by these hydrologic pathways frequently support

the formation of speleothems, which provide long-term archives of changes in Earth's climate on seasonal to multi-millennial timescales (Wong and Breecker, 2015). However, interpreting such time-averaged records requires integration of observational data and simulation studies that provide a temporal bridge between the short-term processes captured in monitoring studies (e.g. seasonal precipitation patterns, temperature fluctuations, vegetation phenology) and the long-term variations (e.g. climate fluctuation, vegetation succession, pedogenesis) recorded by isotopic and geochemical proxies in speleothems. Furthermore, these integrated records are complicated by the variof hydrologic flow paths and attendant hydrogeochemical signatures of fluids transiting from the soil surface to the location of speleothem formation. These factors indicate the utility of models coupling solute transport and reactive transformation in parsing the unique signatures recorded in karst environments.

Although many speleothem studies focus on δ^{18} O reconstructions, speleothem carbon isotope records (δ^{13} C) hold great potential for reconstructing past Critical Zone response to climate change, such as changes in vegetation, soil respiration, carbon stabilization in deep soils, and/or chemical weathering in the host rock (e.g. Dorale et al., 1998; Genty et al., 2003; Polyak et al., 2012; Oster et al., 2015; Fohlmeister et al., 2020). Speleothem δ^{13} C data are easily collected during routine analysis for δ^{18} O, yet the wide range of potentially interrelated factors influencing speleothem δ^{13} C values cause these data to often go unanalyzed and unreported (Fairchild and Baker, 2012). Fluctuations in speleothem δ^{13} C values have been variably interpreted to reflect (1) the ratio of C₃ to C₄ plant species above a cave (Dorale et al., 1998), (2) degassing of CO₂ and precipitation of carbonate along seepage water flow paths and on cave ceilings (Baker et al., 1997; Mickler et al., 2004; Oster et al., 2009; Fohlmeister et al., 2020), (3) the extent of fluid-rock interactions in the host rock (e.g. Hendy, 1971, Genty et al., 2001; Polyak et al., 2012; Oster et al., 2017), (4) climatic and ecosystem controlled variations in soil respiration and/or the relative proportion of soil versus atmospheric CO2 in the dissolved inorganic carbon (DIC) pool (Genty et al., 2001, 2003, 2006; Frappier et al., 2007; Oster et al., 2009; Ersek et al., 2012; Fohlmeister et al., 2020), and (5) long-term variations in atmospheric pCO₂ that influence carbon isotope fractionation in C₃ plants (Breecker, 2017).

Analysis of 14 C content in speleothems offers one strategy for clarifying interpretations of speleothem δ^{13} C values and can provide paleoclimate or geochronologic information of its own (Lechleitner et al., 2016; Fohlmeister and Lechleitner, 2019). The 14 C content of fluids driving speleothem formation is influenced by soil carbon cycling and dissolution of host rocks; however, their influence on cave waters must be considered in the context of speleothem records. For example, studies of 14 C in soils distinguish between several organic carbon pools with characteristically different radiocarbon dynamics (Trumbore, 1993). Correspondingly, the 14 C of CO₂ and dissolved carbon produced from microbial decomposition

of soil organic matter and plant respiration often reflects a disproportionate influence of pools with characteristically shorter residence times (Trumbore, 2009). Records of speleothem ¹⁴C, however, suggest that seepage water DIC in limestone-hosted caves can be derived from both young and old soil carbon, deep vadose zone carbon sources, as well as carbon from the host rock, which is usually radiocarbon dead (Genty et al., 1998, 2001; Genty and Massault, 1999; Oster et al., 2010; Fohlmeister et al., 2011; Rudzka et al., 2011; Noronha et al., 2015). Speleothem ¹⁴C and δ¹³C records have been used to track variations in modern soil carbon turnover rates (Rudzka-Phillips et al., 2013; Carlson et al., 2019) and to infer changes in above-cave soil development that are related to climate change on long (centennial to millennial) timescales (Genty et al., 2001; Oster et al., 2010; Rudzka et al., 2011; Griffiths et al., 2012). However, the potential influence of host rock dissolution on speleothem ¹⁴C suggests that, like δ^{13} C, variations in 14 C could reflect changes that occur below the soil zone that may or may not be linked to climate change (Fohlmeister et al., 2011; Griffiths et al., 2012; Noronha et al., 2014).

Here we describe a strategy for simulating carbon transformations in limestone cave environments and the resultant δ¹³C and ¹⁴C signatures of drip waters. Our objective is to provide new insight into subsurface processes in the karst Critical Zone and to assist the interpretation of speleothem proxies. To do this, we draw upon the rich foundation of numerical reactive transport models (RTMs) which have been increasingly applied to a variety of transport and transformation pathways in the Critical Zone (Li et al. 2017). RTMs integrate fluid flow and transport with a full geochemical thermodynamic and kinetic framework to quantitatively evaluate coupled physical, chemical, and biological processes (Maher and Mayer, 2019; Druhan and Tournassat, 2020). Previous applications of multicomponent numerical RTMs to quantify the partitioning of both stable and radiogenic isotopes have yielded new insight into secondary mineral growth, fluid transport and mechanisms of mixing, terrestrial weathering rates and contaminant fate and degradation pathways (Druhan and Winnick, 2019; Druhan et al. 2019). These isotope-enabled RTMs allow the possibility to bridge spatial and temporal gaps between the scales of what can be observed in a cave system through monitoring and what is recorded in a speleothem proxy record. In this study, we use the soil gasses, soil waters, cave drip waters, and host rock samples from Blue Spring Cave in Tennessee to parameterize and verify a novel RTM of a karst system in order to investigate how fluid flow, dissolution of host rock, and cave-atmosphere connectivity interact to create and alter chemical signatures of surface environmental conditions that might ultimately be preserved in speleothems. This multi-isotope simulation serves as a basis to explore the dominant controls on carbon (δ^{13} C and Δ^{14} C) signatures in cave drip waters and speleothems. In a companion paper (Oster et al., this volume), we extend this approach to the controls on trace elemental signatures in Blue Spring drip waters.

2. SITE CHARACTERIZATION

Blue Spring Cave (35.96°N, 85.39°W, 300 m a.s.l.) is the longest known cave in Tennessee, with ~62 km of mapped passage. Blue Spring was chosen for this study due to its accessibility, the fact that it has been well mapped by the caving community, and the opportunity to sample drip water at multiple locations throughout the cave. Blue Spring is developed within the Mississippian Monteagle Limestone, which is 67-76 m thick in this area. The Monteagle is primarily composed of oolitic and skeletal grainstones and packstones, with the dominant skeletal grains being echinoderm and bryozoan fragments. The cave lies near the contact between the Monteagle Limestone and the Hartselle Formation, which shows evidence of paleoweathering and subaerial exposure in this region (Driese et al., 1994). Blocks of limestone within the cave that likely fell from the cave ceiling appear to display some of the reddening that is characteristic of the weathered contact. Additional petrographic characterization and chemical analysis of the cave host rock are presented in the companion paper (Oster et al., this volume). Portions of the cave farther from the entrance are overlain by Pennsylvanian sandstones and conglomerates that block infiltrating water and keep much of the cave dry (Matthews and Walter, 2010). However, areas near the edges of cave development and not underneath this cap rock are wet and have substantial active speleothem formation.

The climate above Blue Spring is humid subtropical with hot summers and mild winters. Average annual precipitation at the National Climatic Data Center monitoring site in Cookeville, TN (36.11°N, 85.50°W, 332 m a.s.l.) was ~1410 mm/v between 1968 and 2012. Rain falls throughout the year in this part of Tennessee; however the late summer through early fall months tend to be the driest (~20%) annual precipitation from August to October). Vegetation above Blue Spring consists of deciduous hardwood forest, and soils consist of clay loam on top of clay that has been weathered from limestone and sandstone colluvium. Soil thickness above the cave is highly variable and ranges from 0 to >135 cm. Blocks of limestone crop out at the surface or are situated at variable depths below the surface. Mineralogic characterization of soil from above the cave via quantitative XRD is detailed in the companion paper (Oster et al., this volume). Briefly, saprolite and soils consist primarily of quartz (70-88 wt%) with some amorphous phases (11-28 wt%) and small amounts of mica (trace to 2 wt%).

3. METHODS

3.1. Monitoring of surface and cave conditions

Active monitoring has been ongoing at Blue Spring Cave since June 2013. Visits to the cave have been on a monthly to seasonal basis. Monitored observables include surface air temperature and humidity, rainfall amount, and soil temperature and moisture. Within the cave, air temperature, humidity and pCO_2 were measured and logged using a simple non-dispersive infrared sensor

(CO2meter.com, Florida, USA) at four locations throughout the cave at each visit beginning in November 2013 (Figs. 1 and 2).

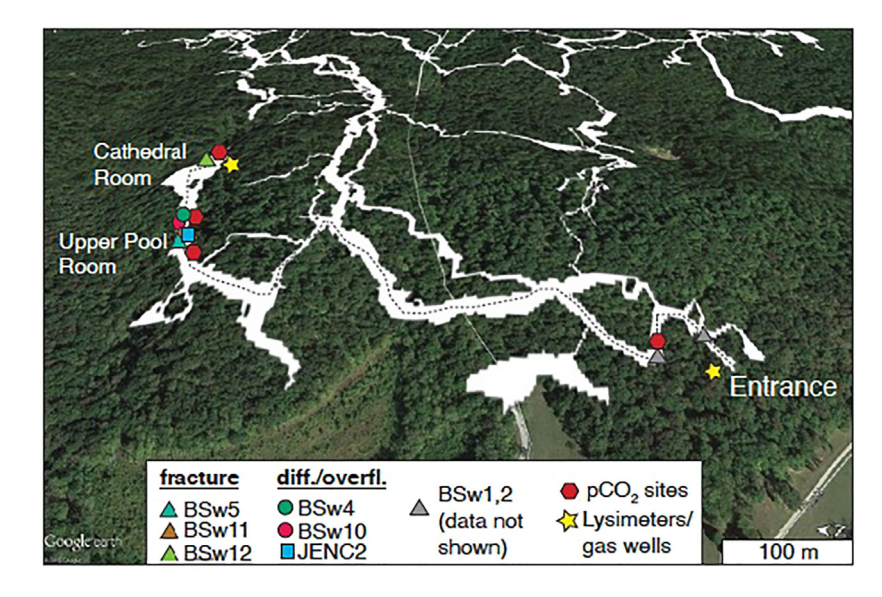
Drip rate has been logged at many of the sample sites within the cave using a combination of Stalagmate acoustic drip rate loggers (Driptych, http://www.driptych.com/, United Kingdom), HOBO tipping bucket rain gauges (Onset, Massachusetts, USA), and homemade Arduinobased "cave pearl" loggers (https://thecavepearlproject.org/). Stalagmate drip loggers were installed at site BSw10 from September 2013 to March 2017 and BSw4 from March 2015 to March 2017 (Fig. 1). A tipping bucket rain gauge used to measure drip rate at the BSw12 from March 2015 to June 2016. Arduino-based loggers were used at sites JENC 2–4, a cluster of close sites in the Upper Pool Room, during spring 2017.

Lysimeters and soil gas wells are installed above the cave at three depths. The main site of soil water and gas monitoring has been coordinated via GPS to be above the Cathedral Room at the end of the typical sampling route within the cave. This location was chosen to maximize the likelihood that lysimeters are capturing water infiltrating through the soil and host rock to the monitored portion of the cave. Lysimeters were installed at soil depths of 30, 50 and 90 cm (L03, L04 and L05, respectively). Gas wells sample soil gas at depths of 40-45, 85-90 and 130-135 cm (BSgw1, BSgw2 and BSgw3, respectively). At a separate location near the cave entrance, two lysimeters were installed at depths of 30 and 70 cm (L02 and L01, respectively) (Fig. 1). Soil temperature and moisture were continuously logged at approximately 25 and 70 cm depth between April 2014 and June 2016 above the Cathedral Room.

Temperature and rainfall in the vicinity of the cave are measured using a HOBO weather station that includes a tipping bucket rain gauge placed at the Cherry Creek Nursery approximately 15 km northwest of Blue Spring Cave. This weather station was operational between December 2013 and March 2017. In August of 2014, another weather station was established just 1 km from the cave. Net rainfall is calculated for both sites, taken to be the difference between precipitation measured at the weather station and potential evapotranspiration, calculated using the Thornthwaite equations after Willmott et al. (1985) and Tremaine and Froelich, (2013). Net rainfall is generally higher and positive during the winter months and negative for much of the summer and fall.

3.2. Water and gas sample collection and analysis

Drip water was sampled monthly to seasonally at multiple locations within the cave and analyzed for $\delta^{18}O$, $\delta^{2}H$, $\delta^{13}C_{DIC}$, pH, and cation concentrations. Drip sites that display differing flow characteristics were specifically targeted, including those displaying intermittent and continuous flow, in order to sample a variety of flow paths through the soil and host rock. Water drips occur seasonally near the cave entrance, and sites BSw1 and BSw2 were sampled intermittently in this part of the cave beginning in June 2013 (Fig. 1). Site BSw2 became inactive after February



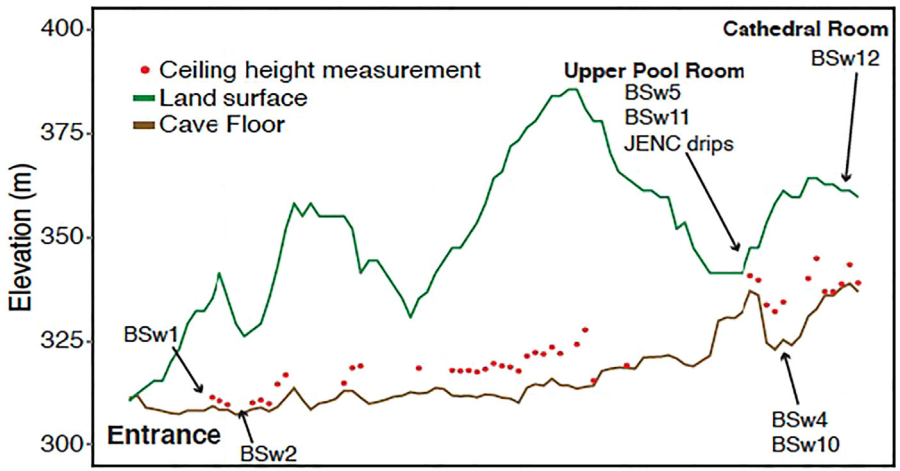


Fig. 1. (A) Partial map of Blue Spring Cave overlain on Google Earth image. Dashed line shows route taken for water sampling within the cave. Sites for water sampling and pCO₂ monitoring within the cave are marked, as are surface lysimeter installations. Cave map is adapted from J. Richards (https://www.rchrds.org/tennesseecarto/2018/1/9/blue-spring-cave). (B) Profile of cave along sampling route shown in top panel (in m a.s.l.). Measurements of land surface and cave ceiling height from cave cartography work of J. Richards are shown as are sampling sites. Data from water sampling sites BSw1 and BSw2 are not further discussed in the text because these sites became dry partway through the study.

2015 when an ice storm appears to have led to changes in water flow routes that caused this drip location to become dry. The majority of water sample sites are located near the end of the sampling route in the Upper Pool Room, front Cathedral Room, and back Cathedral Room (Fig. 1). Site BSw5 in the Upper Pool Room was sampled from June 2013 through May 2017. Also in the Upper Pool Room, site BSw11 was sampled from August 2014 through November 2017. Sites BSw4 and BSw10, located in the front Cathedral Room were sampled from June 2013 through November 2017, and site BSw12, a very slowly dripping site in the back of the Cathedral Room, was monitored from May 2015 through March 2017. Lastly, sites JENC1 – JENC4 in the Upper Pool Room were sampled several times during winter and spring 2017 as part of a targeted effort to investigate spatial heterogeneity in drip rate and water chemistry within a single room of the cave.

Drip water was collected instantaneously at each drip site into precleaned LDPE bottles and then subdivided for each analysis type. At slower drip sites, LDPE bottles were left under the drip at the beginning of the sampling trip and collected on the return trip out of the cave. No bottle was left for more than 1 hour, and no calcite precipitate was ever observed within a collection bottle. Water was extracted from the soil lysimeters on a monthly to seasonal basis using a handheld vacuum pump. Water samples for O and H isotope analysis were stored in acid-cleaned 20 ml LDPE vials and capped with minimal headspace to reduce the potential for evaporative bias. Water samples for carbon isotope analysis of DIC were filtered through 0.2 micron sterile filters. Filtered waters (2 ml for drip waters and 3 ml for soil waters) were then injected into heliumflushed 12 ml rubber septum-capped Labco Exetainer® vials containing 1 ml phosphoric acid. Water samples were

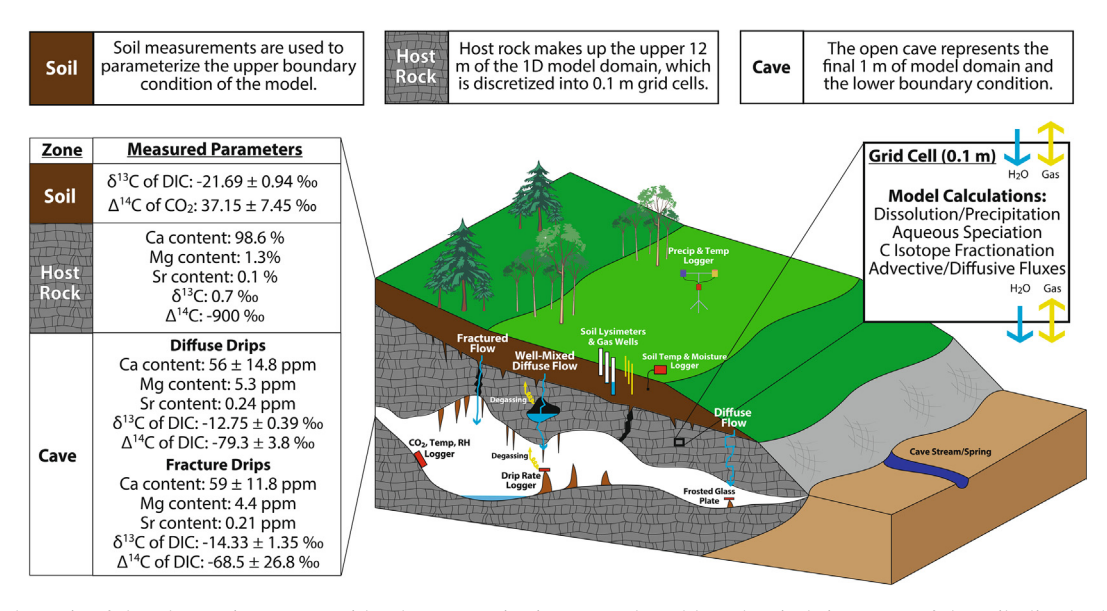


Fig. 2. Schematic of the Blue Spring system with relevant monitoring network and key chemical signatures of the soil (dissolved inorganic carbon isotopes), host rock (limestone composition), and cave drip water (major and trace element concentrations and carbon isotopes). The model domain spans a 1D depth profile 13 m in length, including 12 m of host rock from the base of the soil to the ceiling of the cave, and 1 m of open cave air, thus directly simulating infiltration of soil water, dissolution of limestone, and formation of secondary carbonates resulting from rapid degassing of CO₂.

kept refrigerated until analysis. Samples were stored for a maximum of 6 months. Water samples for cation analysis were similarly filtered then acidified with concentrated trace metal grade nitric acid on the surface following pH measurements. Soil gas was collected on a seasonal basis beginning in summer 2014. Approximately 3 ml of soil gas was injected into 12 ml helium-flushed rubber septum-capped Labco Exetainer[®] vials onsite after purging the approximate well volume using a 50 ml luerlock syringe two times.

Soil gas and water samples were analyzed for $\delta^{13}C_{DIC}$ at the UC Davis Stable Isotope Facility using a Thermo Finnigan Delta V Plus IRMS coupled to a GasBench II. Evolved CO₂ was purged from the Labco vials through a double-needle sampler into a helium carrier stream (20 mL/min). The gas was sampled using a six-port rotary valve (Valco, Houston TX) with either a 100, 50 or 10 μL loop programmed to switch at the maximum CO2 concentration in the helium carrier. The CO₂was passed to the IRMS through a Poroplot Q GC column (25 m \times 0.32 m m ID, 45 °C, 2.5 mL/min). A reference CO₂ peak was used to calculate provisional delta values of the sample CO₂ peak. Final δ^{13} C values are obtained after adjusting the provisional values for changes in linearity and instrumental drift such that correct δ^{13} C values for laboratory reference materials are obtained. At least 2 laboratory reference materials were analyzed with every 10 samples. Laboratory reference materials are lithium carbonate dissolved in degassed deionized water and a deep seawater (both calibrated against NIST 8545). Final δ^{13} C values are expressed relative to the international standard V-PDB, with a longterm standard deviation on δ¹³C analyses of CO₂ and DIC of 0.1%.

Water samples for O and H isotopes were analyzed at the SIRFER lab at the University of Utah using a ThermoFinnigan Delta Plus XL isotope ratio mass spectrometer. All delta values are reported in permil notation relative to V-SMOW. Standard deviation on standards analyzed during analysis was ≥ 0.2 for $\delta^2 H$ and 0.04 for $\delta^{18} O$. Calcium (Ca) concentrations in soil water and drip water were measured in solution mode on a Thermo Finnigan iCapQ at Vanderbilt University. Concentration standards were prepared using a custom mixed solution from Inorganic Ventures (Christiansburg, VA) containing Na, Ca, and Mg. These were mixed online with an internal standard solution (IV-71D). The standard solution IV-Stock-10 was run as an unknown during each analysis period.

Radiocarbon in soil and cave water DIC and air was measured six times throughout the study period, in spring and fall 2015; spring, summer and fall 2016; and winter 2017. Soil water for radiocarbon analysis was collected from the deepest lysimeter (L05). Drip water was collected from sites BSw4, 5, 11, and 12. During the dry fall of 2016, it was only possible to collect a sufficient amount of water at site BSw4. All water samples were collected in precleaned and baked 100 ml Pyrex vials, capped with no headspace, and refrigerated until analysis. Soil gas was collected for radiocarbon analysis from the deepest gas well (BSg3) in fall 2015 and 2016, summer 2016, and winter 2017. Cave air was collected from the Cathedral Room in fall 2015. Air samples were collected in evacuated stainless steel Restek vacuum cannisters. Samples were sent to the W. M. Keck Carbon Cycle Laboratory at UC Irvine where DIC samples were sparged with phosphoric acid and evolved CO₂ was purified and then converted to graphite for analysis by accelerator mass spectrometer. All radiocarbon data are presented as Δ^{14} C notation. Sample preparation backgrounds have been subtracted based on measurement of 14C-free DIC made from calcite. Results are corrected for isotopic fractionation according to the conventions of Stuiver and Polach (1977) using $\delta^{13}C$ values measured on prepared graphite using the accelerator mass spectrometer.

3.3. Batch limestone dissolution experiments

The construction of an RTM simulation in application to a specific natural system requires constraint of multiple input parameters (discussed further below, Section 4.2). An important class of these required input parameters are constraints on the limestone composition and chemical reactions that solubilize this solid phase appropriate for the Blue Spring system. Often, these parameters are not known in advance, as commonly available thermodynamic databases (e.g. EQ3/6, Wolery and Daveler, 1992) largely contain generic pure mineral endmembers rather than the unique composition of a given limestone such as the Monteagle which hosts Blue Spring. Many specific applications thus strive to constrain the composition and chemical parameter values of an appropriate representative carbonate, such as in the marine diagenesis model developed by Maher et al. (2006).

For the present study, we undertook a batch dissolution experiment using a rock sample collected from within Blue Spring Cave to directly constrain reaction rate parameters appropriate to this environment. A sample of the Monteagle Limestone collected from a cave ceiling breakdown block was cut to a cubic shape to reveal fresh unweathered surfaces. Total surface area was directly measured as 47.9 cm². The initial dry mass of the sample was 66.924 g. This sample was suspended in 1100 mL of ultrapure deionized (DI) water (pH = 5.3) at a fixed temperature of 22 °C and the solution was continuously stirred using a magnetic stir bar. The solution pH was continuously monitored and small volumes of fluid sample were collected periodically over the course of 24 hours, immediately filtered (0.2 μm), and acidified with trace metal grade nitric acid to a final concentration of 2%. Cations were measured by inductively coupled plasma mass spectrometry at the University of Illinois Urbana-Champaign.

4. REACTIVE TRANSPORT MODEL CONSTRUCTION

4.1. Overview

We construct a multicomponent reaction model using the open source CrunchTope software (Druhan et al. 2013; Steefel et al. 2015). Development of a CrunchTope model appropriate to Blue Spring requires specification of multiple parameters which are used to solve an overall governing equation of the form:

$$\frac{\partial C}{\partial t} = -v \frac{\partial C}{\partial x} + D \frac{\partial^2 C}{\partial x^2} + R \tag{1}$$

This formulation would be appropriate to solve for the concentration(s) of dissolved solute(s) or gas phase(s) (C) through time (t) across a one-dimensional domain (x) subject to fluid velocity (v), mixing along concentration

gradients due to diffusion/dispersion (D) and any number and variety of chemical reactions encapsulated by the term (R). This model structure is unique to that of models previously applied to resolve drip water chemistry in cave systems (e.g. Hendy, 1971; Fohlmeister et al., 2011), in which fluid drainage rate is omitted and reactivity is limited to carbonate equilibria (discussed further below). However, Eq. (1) may become more familiar to karst applications when it is adapted from this generic form. For example, Cerling (1984) essentially started from this structure in developing a quantitative description for depth-resolved soil pCO₂ and δ^{13} C signatures by assuming (1) steady state $(\frac{\partial C}{\partial x} = 0)$; (2) no advection (v = 0); and (3) scaling the soil carbon respiration rate (R_s) by an e-folding length to create a characteristic decrease with depth $(R = R_s \times e^{-\frac{x}{x^*}})$ where x^* is a characteristic length scale appropriate to a soil depth profile. The result is the familiar expression (Cerling, 1984; Quade et al. 1989; Cerling et al. 1991):

$$0 = D\frac{\partial^2 C}{\partial x^2} + R_s \times e^{x/x^s} \tag{2}$$

The approaches of Hendy (1971) and Fohlmeister et al. (2011) are distinct from Eq. (1) in that the assumption of steady state is implicitly embedded into the calculations. These models begin with either an initially soil pCO₂-equilibrated fluid (closed system) or one that is fixed in equilibrium with soil pCO₂ (open system) and proceed to calculate the resulting carbonate equilibria and attendant δ^{13} C values, while satisfying charge balance by addition of an appropriate amount of Ca²⁺ to achieve electroneutrality. This addition of a cation is intended to represent the solubilization of limestone, and the evolution of the system is achieved by incrementally increasing pH and repeating the calculation until equilibrium with solid phase CaCO₃ is achieved.

In comparison, the RTM presented here differs in two ways. First, the treatment of water–rock reactivity that solubilizes limestone includes a kinetically limited reaction rate law (discussed further Section 4.2). Second, the velocity at which fluid drains through the host rock is explicitly implemented in the calculation (discussed further Section 4.6). These two features of the model introduce two characteristic timescales, one associated with the rate of fluid flow, and the other associated with the rate of reactivity.

4.2. Reactivity

The term *R* in Eq. (1) may be expanded to encapsulate a wide variety of equilibrium and kinetic reactions depending upon model application (Steefel et al. 2015; Li et al. 2017; Maher and Mayer, 2019). The collective set of these reactions are then solved numerically as a differential–algebraic set including both time-dependent kinetic reactions (differential) and instantaneous equilibria (algebraic) subject to ion activity corrections using a Debye-Huckel activity model (Steefel et al. 2015). For the present study, we employ a suite of equilibrium reactions and a single kinetic rate expression describing limestone solubilization. Equilibrium reactions include:

$$OH^- + H^+ \leftrightarrow H_2O \tag{3}$$

$$CO_3^{2-} + H^+ \leftrightarrow HCO_3^-$$
 (4)

$$CO_{2(aa)} + H_2O \leftrightarrow HCO_3^- + H^+ \tag{5}$$

$$CO_{2(g)} + H_2O \leftrightarrow HCO_3^- + H^+ \tag{6}$$

$$CaOH^{+} + H^{+} \leftrightarrow Ca^{2+} + H_{2}O \tag{7}$$

$$CaCO_{3(aq)} + H^+ \leftrightarrow Ca^{2+} + HCO_3^- \tag{8}$$

$$CaHCO_3^+ \leftrightarrow Ca^{2+} + HCO_3^- \tag{9}$$

The corresponding temperature-dependent equilibrium constants are provided in supplementary information (Table S1). The kinetic rate expression for limestone dissolution utilizes a transition state theory (TST) rate law (Lasaga, 1981), which describes a kinetically limited approach to equilibrium:

$$\frac{\partial C}{\partial t} = kA \left(1 - \frac{Q}{K_{eq}} \right) \tag{10}$$

where the rate of the reaction is determined by a rate constant (k), a mineral reactive surface area (A), and the departure of the system from equilibrium, represented as the difference between unity and the ratio of the ion activity product (Q) and the equilibrium constant for the reaction (K_{eq}) . The value of Q at any given time is defined in the same manner as the equilibrium constant for the reaction but based on the solution composition at that moment. The stoichiometry of the dissolution reaction follows the overall form:

$$CaCO_{3(s)} + H^{+ \stackrel{K_{eq}}{\longleftrightarrow}} Ca^{2+} + HCO_{3}^{-}$$
 (11)

But we recognize that the particular composition of the Blue Spring host rock will include components of Mg^{2+} , Sr^{2+} and other divalent cations which will cause the reactivity and associated model parameters to diverge from that of pure calcite (Section 5.3; Oster et al., this volume). As in Hendy (1971) and Fohlmeister et al. (2011), only a subset of the species listed in Eqs. (3)–(9) actually needs to be defined at the start of the simulation in order to solve for the rest. These "basis" species for the present model are H^+ , HCO_3^- and Ca^{2+} and are input to the model as total concentrations (Lichtner, 1985; Morel and Hering, 1993) for all initial and boundary conditions.

It is useful to note that this set of kinetic (Eq. (10)) and equilibrium (Eqs. (3)–(9)) reactions may be applied to a variety of different environmental conditions. For example, dissolution of limestone may occur in a closed system with a fluid that is initially in equilibrium with atmospheric CO₂, as for the batch reaction experiments (Section 3.3). Dissolution of the same limestone may also occur in the open system of the Blue Spring karst, where fluid is through-flowing and nominally equilibrated with a higher soil pCO₂ deriving from respiration of organics. In either instance, the equations provided above can adjust to accommodate these unique environments. The differences between these two systems manifest in the ion activity product (Q) of Eq. (10), as a result of the H⁺, HCO₃ and Ca²⁺concentrations of the given system (Eqs. (3)–(9) and (11)), but do not inherently alter the intrinsic rate constant of the reaction (k) or the mineral reactive surface area (A). Therefore, a rate constant constrained by applying Eq. (10) (and associated equilibria Eqs. (3)–(9)) from the batch reaction experiments can be subsequently utilized to model dissolution of the same limestone in the more open Blue Spring environment, subject to the unique chemical conditions of this system. The key point is that the application of this stoichiometrically based modeling approach allows the constraint of a necessary parameter value in the laboratory which may then be translated to the field (Section 5.3.1).

4.3. Carbon isotopes

The reactions used to describe carbon and limestone dynamics are the same as described in Section 4.2, with equilibrium parameters appropriately adjusted to an average temperature of 13.5 °C (i.e. the MAT above Blue Spring Cave) using a polynomial fit between 0-300 °C implemented in the CrunchTope software (Steefel et al., 2015). However, the isotopes of carbon are each explicitly simulated as individual 'species' which are distributed in appropriate ratios based on the δ^{13} C values and radiocarbon compositions measured at Blue Spring. In other words, each equilibrium expression (Eqs. (3)–(9)) is repeated three times, to include all three isotopes of carbon. Similarly, the rate expression (Eq. (10)) is solved three times in each timestep to simultaneously track the three isotopes during limestone dissolution. This requires that the limestone stoichiometry (Eq. (11)) be updated to reflect the distribution of carbon isotopes:

$$CaCO_3^+H^+ \stackrel{K_{eq}}{\longleftrightarrow} Ca^{(2+)} + 0.988879999999991^{12}CO_3^- + 0.01112H^{13}CO_3^- + 0.0000000000011H^{14}CO_3^-$$
 (12)

where the limestone mineral (CaCO₃) is composed of three isotopes of carbon represented by the three unique carbonate mole fractions on the right side of the equilibria. The resulting radiocarbon value (Δ^{14} C) is -900% and the δ^{13} C value is 0.7‰. Minor differences in the equilibria among the isotopes can be utilized to introduce stable isotope fractionation. This is done using a simple linear relationship originally reported by Mook et al. (1974) and subsequently adopted by several others (e.g. Mook, 1986, 2000, Zhang et al., 1995; Drevbrodt and Scholz, 2011). Fractionation is included between dissolved species HCO₃ and $CO_{2(aq)}$ ($\varepsilon = 8.94\%$ at 25 °C); HCO_3^- and CO_3^2 $(\varepsilon = 0.39\%$ at 25 °C); HCO₃ and CaCO₃ ($\varepsilon = -2.40\%$ at 25 °C); and between aqueous and gas phase CO₂ $(\varepsilon = 1.06\%$ at 25 °C), with corresponding temperature dependent adjustments. This multi-isotope simulation of carbon was recently benchmarked in a numerical modeling exercise (Druhan et al., 2020a) and the present formulation follows the same approach.

4.4. Physical properties

We base the size and structure of the 1D reactive transport simulation on information gained from extensive surveying within this cave system (J. Richards, https://www.rchrds.org/tennesseecarto/2018/1/9/blue-spring-cave).

Cave passages have been carefully mapped and georeferenced to the entrance; thus, we are able to estimate the thickness of overburden along our sampling route within Blue Spring (Fig. 1). Based on this information and our soil depth measurements, we estimate ~10–15 m of limestone overlies the portions of Blue Spring Cave from which the majority of our drip water samples are collected. Thus, we conduct our simulation along a 1D depth profile spanning 13 m and discretized into 0.1 m intervals, in which the first 12 m are composed of the partially saturated limestone, and the bottom 1 m is effectively open air reflecting the cave interior (Fig. 2).

The model domain is defined such that the upper boundary condition is fixed to the measured conditions reported for soils monitored above the cave system (Section 5.1) and the lower boundary condition is the open cave. The model domain represents the distance between the base of the active soil layer and the ceiling of the cave (Fig. 2), including a small portion of the upper cave chamber. From the top to 12 m depth across the domain, the initial condition includes a uniform volume fraction of 0.3 limestone. The remaining space is open, resulting in a starting porosity of 70%, of which water saturation is set to 20%, such that the remaining 80% of open pore space is occupied by gases including O₂ and CO₂. The last meter of the domain (12-13 m depth) is fixed to a porosity of 99% to mimic the ceiling of the cave. Since true values for water saturation and porosity are unknown, we start with these reasonable estimates and subsequently evaluate the sensitivity of the model to these parameters (Section 6.4). We do not explicitly treat gas phase advection in the simulation as this would present an additional unknown parameter describing the gas flow rate for which we have essentially no constraint. Rather, the large available porosity and low water saturation support the use of a free air diffusion coefficient, which we set to a value of 0.16 cm²/s as appropriate for $CO_{2(g)}$ (Jabro et al. 2012). This gas diffusivity is much larger than typical values employed in RTMs focusing on transport in porous media (Steefel and Maher, 2009) which are commonly corrected for tortuosity or other metrics of pore connectivity. Thus, the simulation described here supports abundant interaction between the gas phases occupying the karst and the upper boundary condition, facilitating communication between the model domain and the atmosphere. However, we emphasize that this approach does not inherently define the system as 'open' or 'closed' in the sense of the Hendy (1971) or Fohlmeister et al. (2011) models. As will be shown below, connectivity between the gas in the karst interior and the overlying boundary condition is necessary to reproduce the observed distribution of reactivity and the observed carbon isotope values of DIC in this system (Section 5.4).

4.5. Boundary conditions

The upper boundary condition of the simulations is adjusted such that the dissolved inorganic carbon composition (Section 4.3) is specified in equilibrium with a fixed soil pCO₂ value, and charge balance is used to constrain the associated pH. This boundary value dictates the reactivity

of fluid entering the top of the model domain and can be constrained based on samples from our lysimeters and gas ports (Section 5.1). As will be shown, the pCO₂ of the soil above Blue Spring varies substantially with season, thus creating a key variable which will dictate changes in the reactivity of fluid infiltrating the karst. Thus, we define the upper boundary condition soil pCO₂ as the first of two "principal parameters" in the model, meaning that we do not fix it to a single value, but rather proceed in all subsequent 1D simulations using three scenarios of low, medium, and high pCO₂ (Section 5.1.1) based on our observational data. The 1D simulation also requires a second boundary condition at the base of the domain, corresponding to the conditions of the cave atmosphere in approximately the location of the Blue Spring Cathedral Room. We consider the effect of entering the open cave in the last meter of the domain by increasing the porosity to 99% in these grid cells. This approach serves two purposes. First, it causes the fluid drainage rate to slow down to approximately 1% of the value in the karst, as would be expected of water emerging along a cave ceiling and collecting into drips. Second, it creates a large gas-phase reservoir representative of the cave airspace.

Notably, the fluid chemical composition of this lower boundary condition is not influential to the present results. as all fluid flow moves from top (base of soil) to bottom (open cave); thus, no fluid is introduced into the system from this lower boundary. However, the gas phase composition of this boundary condition could be relevant, as it mixes with the partially saturated gas within the overlying karst and may thus exert an influence on fluid phase composition. For the present model, we begin by establishing a "base case" simulation in which this gas phase interaction is omitted by setting a Neuman boundary condition. In this scenario, the model results reflect a condition in which the cave air does not impact the solution chemistry of fluid draining through the overlying host rock (Section 6.4). Building upon this basis, we subsequently explore two examples of a fixed gas phase boundary condition (Dirichlet) including a lower pCO₂ of 0.8% used to represent values typical of winter months and a higher pCO₂ of 1.5% used to represent values typical of summer months in the Cathedral Room (Fig. 3). These cave air effects are further described in Section 6.3.

4.6. Flow rate

Perhaps the least constrained parameter is the drainage rate of fluid through the karst. Drip rates recorded in the cave interior (Section 5.2.1) provide a useful starting point; however, conversion of these values into fluid velocities requires significant assumptions. This leads us to define the second of our principal parameters in the model, proceeding with all subsequent 1D simulations using three values of slow, moderate and fast flow rates (Section 5.2.1) based on what we can infer from the drip rates. In total, the combination of three soil pCO₂ values and three flow rates results in nine individual simulations that constitute what we refer to as our 'base case' model results. We then evaluate

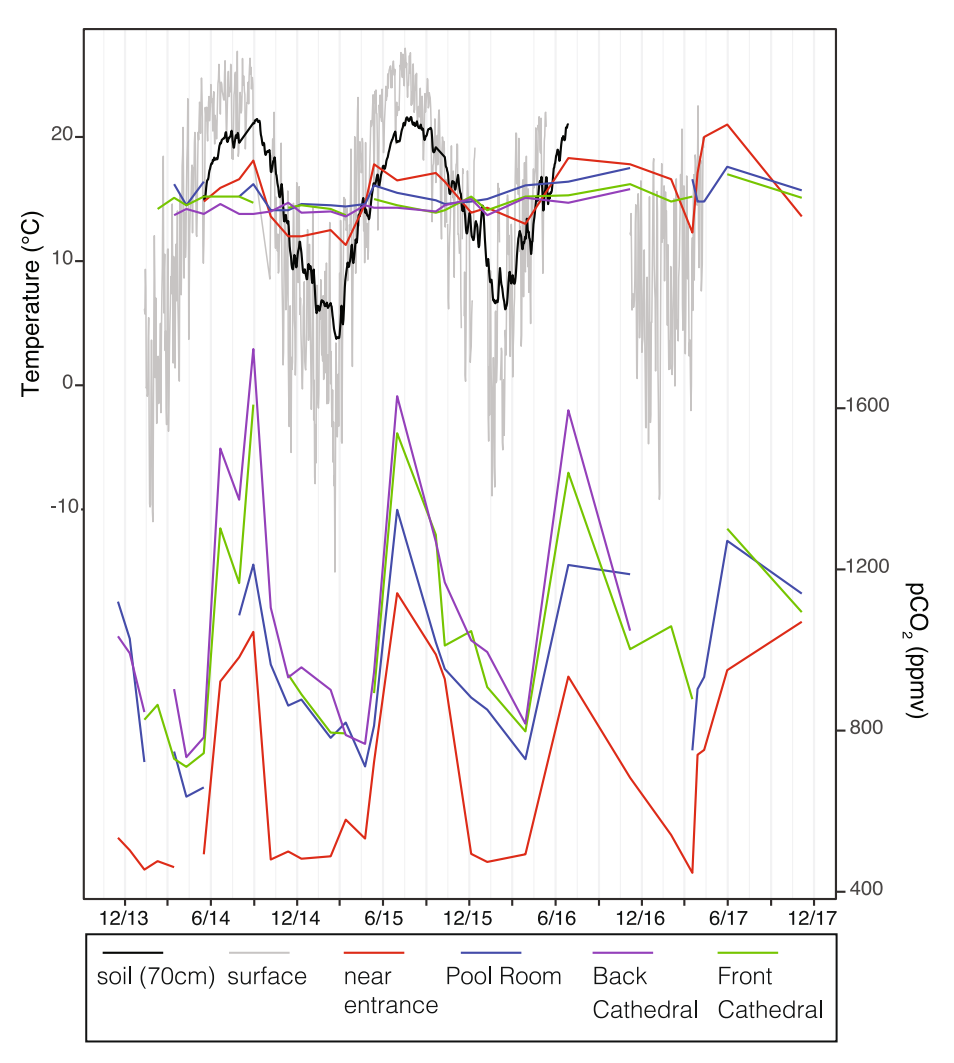


Fig. 3. (A) Average daily air temperature measured at the Cherry Creek weather station (gray line) and average daily soil temperature at 70 cm depth above the Cathedral Room (black line) compared with point measurements taken at several locations within the cave. In order of increasing distance from the entrance, these are named near entrance (red), Pool Room (blue), front Cathedral Room (green), back Cathedral Room (purple) – see red symbols in Fig. 1 for locations). (B) Point measurements of cave air pCO₂ taken at the same locations as the temperature measurements. (For interpretation of the references to color in this figure legend, the reader is referred to the web version of this article.)

the response of our model results to further variability in these parameters through a series of sensitivity tests (Section 6.4).

4.7. Summary of modeling approach and parameters

Many of our model parameters are taken from the literature (e.g. carbonate species equilibrium constants, radiocarbon half-life, stable isotope fractionation factors). Some are constrained based on direct observations from our field work and associated sample analysis, as well as the batch reaction experiments. Those that remain poorly constrained and of key significance to the model results are treated as principle parameters and a range of values are explored. This approach is summarized in Table 1 and encapsulates our best efforts to constrain the model based on our knowledge of the Blue Spring site. We refer to this as our base case set of simulations. We then evaluate

the sensitivity of model results to even greater variations in these parameters (Section 6.4).

5. RESULTS

5.1. Surface conditions and cave air

Local weather conditions were consistent with the regional climate. Average daily temperature at the monitoring site varied from ~0.5 °C during the winter to 26 °C during the summer; however, the 2016–2017 winter season was warmer and more variable than the previous years (Fig. 3). Soil temperature displays the same seasonality, with temperatures ranging from 2 to 22 °C at 35 cm depth and 4–21 °C at 70 cm (Fig. 3). Cave air temperature shows a much narrower range of seasonal variability (~2 °C at the back of the Cathedral Room and ~10 °C near the cave entrance, Fig. 3). Cave air pCO_2 is lowest near the cave

Table 1
Model input parameters and guide to relevant sections in the manuscript for detailed explanations.

Source	Parameter	Description
Literature-derived	Carbonate equilibria	Supplementary Info
	δ ¹³ C fractionation factors	Section 4.3
	¹⁴ C half-life	Section 4.3
	Gas phase diffusivity	Section 4.4
Observationally Constrained	Model domain size	Section 4.4
	Temperature	Section 5.1
	Porosity*	Section 5.1
	Fluid saturation*	Section 5.1
	Soil water chemistry, δ^{13} C & Δ^{14} C	Section 5.1
	Limestone δ^{13} C & Δ^{14} C	Section 4.3
Experimentally Constrained	Limestone dissolution rate constant	Section 5.3.1
•	Limestone equilibrium constant	Section 5.3.1
	Limestone surface area	Section 5.3.1
Primary Parameters [†]	Soil pCO ₂ *	Section 5.1.1
-	Fluid drainage velocity*	Section 5.2.1

^{*} Parameters subject to sensitivity testing in Section 6.4

entrance, where it reaches near-surface values (~400 ppm) in the winter. Cave air pCO_2 increases with distance from the cave entrance, reaching up to 1600 ppm during the summer months in the Cathedral Room at the end of the sampling route, which is also the end of this branch of the cave system. The δ^{13} C value of cave air CO₂ was analyzed three times (October 2015 and March and June 2016) in two locations (near drip sites BSw5 and BSw12). At both locations, cave air δ^{13} C values were lowest when pCO₂ was highest. At the rear of the cave (the Cathedral Room), the minimum cave air δ^{13} C value occurred during June 2016 (-21.2%) (Fig. 4; Table S2). The cave air δ^{13} C in the Pool Room near the location of BSw5 was lowest during October 2015 (-20.2%). Cave air from the Cathedral Room analyzed for radiocarbon in October 2015 reflected a modern ¹⁴C age (Δ^{14} C = 24.2 \pm 1.5). The pCO₂ in this location at the time of collection was 1168 ppmv.

Soil CO₂ increases above Blue Spring during the summer through mid-fall and is lower during the winter and spring months. Soil CO₂ generally increases with depth in the soil, in particular during the growing season (Fig. 4). The δ^{13} C values of soil CO₂ generally varies between -20.5 and -24.9%. Two much less negative values (>-15‰) from samples collected in March 2016 and February 2017 (gray symbols, Fig. 4B) that are also associated with low measured pCO₂ might reflect sample contamination with atmospheric CO₂. Disregarding these samples, the δ^{13} C values of soil CO₂ are generally highest during the winter months. Soil CO₂ from the deepest gas well reflected a modern ¹⁴C age in all seasons (Δ^{14} C ranged from 1.7 to 5.8‰).

For the set of lysimeters located above the Cathedral Room, the $\delta^{13}C_{\rm DIC}$ value of L03 (depth = 30 cm) ranges from -17.9 to -18.8%, L04 (depth = 50 cm) ranges from -19.5 to -22.8%, and L05 (depth = 90 cm) ranges from -19.8 to -23.4% (Table S3). The lowest soil water $\delta^{13}C_{\rm DIC}$ values occur during the winter months. This is in contrast to soil CO_2 which displays slightly higher $\delta^{13}C$ values

during the winter months (Fig. 4). Similar to the soil gas, the Δ^{14} C of the water collected from the deepest lysimeter (L05) reflects a modern ¹⁴C age in all seasons but shows higher values than the soil gas (31.8–47.6‰). The soil water Δ^{14} C was highest during the spring months (March 2015 and 2016) (Fig. 5).

5.1.1. Model constraint: Soil boundary condition

The appropriate value of soil pCO₂ is highly variable in the soil monitoring stations and shifts as a function of season and water saturation, ranging from as low as ~700 ppmv in winter to greater than 30,000 ppmv in warmer and wetter periods in the deepest soil gas well (130-135 cm below soil surface). This variability delineates a principal parameter in our model (Table 1), and the three values of soil pCO₂ are specified as low (0.4%), moderate (1.5%), and high (3%) assuming a total pressure of 1.0 atm for the upper boundary condition. These simulations result in an initial pH of the fluid draining into the limestone from the base of the soil of 6.730, 6.157, and 5.857, respectively. Furthermore, the Ca concentration of the upper boundary is set to an appropriate value draining from the soil (15 ppm) based on measured Ca concentrations in soil waters above Blue Spring. In total, this results in infiltrating fluids that are undersaturated with respect to the host rock by $\Omega = -1.67$, -2.24, and -2.54, respectively, as a function of the pCO₂ boundary condition chosen. Upper boundary condition radiocarbon compositions are all modern (Δ^{14} C of approximately +32‰), and the δ^{13} C value of DIC is -21.8%, also based on measured soil water DIC values from the deep lysimeters (L04, L05) (Fig. 5).

5.2. Cave drip water behavior

Rainfall and drip rate monitoring suggests that drip rates are capable of responding to rainfall on the surface within approximately 24 hours (Fig. S1), but that the timing

[†] Two primary parameters are identified, which exert significant control on the model results for drip water chemistry. We utilize our observational data to arrive at a range of values for these two parameters encapsulating the variability we observe at Blue Spring.

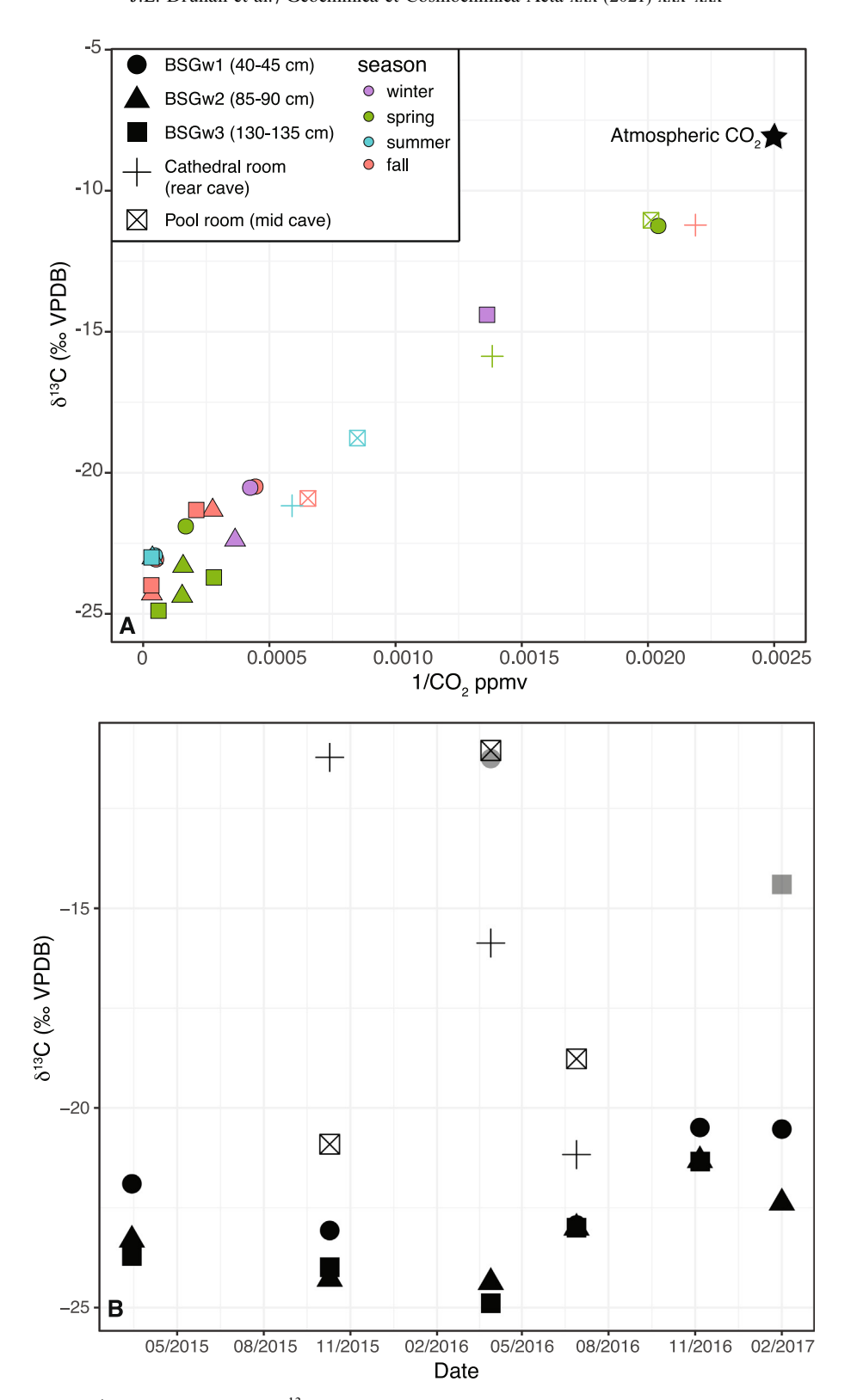


Fig. 4. (A) Keeling plot of $1/CO_2$ concentration vs. $\delta^{13}C$ of cave air and soil gas at three depths, colored by season, with a representative value for atmospheric CO_2 (star). (B) Time series of soil gas and cave air $\delta^{13}C$ measurements. Gray symbols have possible contamination with atmospheric CO_2 and thus are not considered to be representative of soil CO_2 .

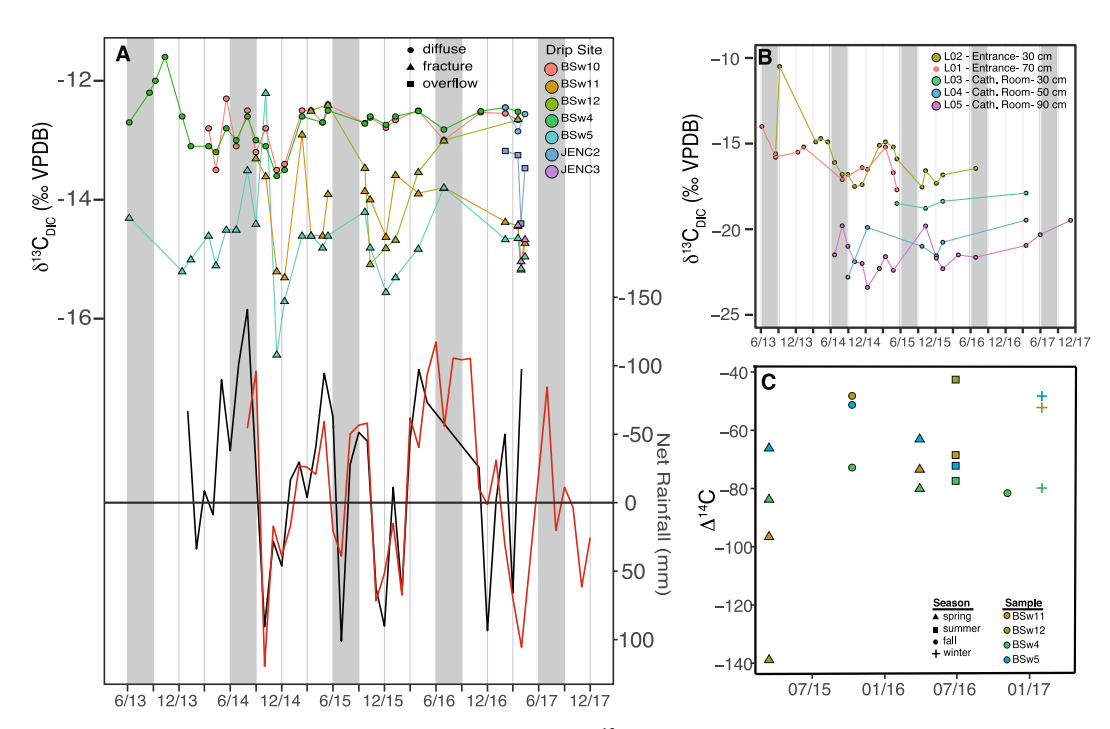


Fig. 5. Carbon isotopes in soil and drip water DIC: (A) Variations in the δ^{13} C of drip water DIC, coded by drip type (e.g. fracture vs. diffuse) with time series of net rainfall calculated based on the Cherry Creek weather station (black) and the Blue Spring weather station (red). Note reversed axis on net rainfall plot. (B) Variations in the δ^{13} C values of soil water DIC at multiple depths at two sites, one near the cave entrance and the second above the Cathedral Room at the end of the sampling route (see Fig. 1). Summer months (JJA) are highlighted in gray in both A and B. C) Δ^{14} C of DIC at four drip sites, coded by distinct symbols. (For interpretation of the references to color in this figure legend, the reader is referred to the web version of this article.)

and magnitude of drip rate responses to rainfall events are highly variable. Monitored drip sites within Blue Spring Cave display three main types of behavior identified based on drip rate and water chemistry. As with surface rainfall, drip rates throughout the cave tend to slow during the late summer and early fall. We refer to drip sites that display a large range of drip rates, respond rapidly to rainfall events, and become seasonally dry as fracture fed drips (BSw5, BSw11, BSw12, JENC3, JENC4). As a point of reference, fracture fed drips have exhibited volumetric flow rates as high as 200 ml/min. Drips that do not seasonally dry up and display more gradual variations in drip rate are referred to as diffuse flow drips (JENC1, BSw4, BSw10). As a comparison, these diffuse drips have been observed to produce flow rates of 5–10 ml/min. These values are consistent with the 'group 1' seasonal drip rates reported by Miorandi et al., (2010) for a cave system located in a Mediterranean climate. Lastly, drip site JENC2 displays what we characterize as an overflow drip, with behavior showing smaller and more gradual responses to some rainfall events, but much larger changes in drip rate in response to large or sustained rainfall events, possibly as a result of reservoir overflow somewhere along the flow path (Fig. S1).

Drip character can also be distinguished on the basis of chemical variability, as fracture-fed drips show a wider range of variability in δ^{18} O, δ^{2} H, and δ^{13} C_{DIC} values (Figs. 5 and 6; Table S2). The δ^{18} O of soil water collected from lysimeters ranges from -4.2 to -7.5% (VSMOW), with generally higher values of soil water δ^{18} O occurring

in the fall dry season (Fig. 6A). Although we were only able to analyze monthly average rainfall $\delta^{18}O$ a few times over the course of the study due to difficulties with the collector, the soil water $\delta^{18}O$ falls within the range of measured rainwater $\delta^{18}O$ values (-4.2 to -8.7‰, n = 7) (Fig. 6B). Drip water $\delta^{18}O$ displays a smaller range of variation (-5.2 to -6.7‰); however, fracture fed drips show a larger range of variation (-5.2 to -6.6) than diffuse drips (-5.3 to -6.4) (Fig. 6B), in particular showing lower $\delta^{18}O$ values during the rainier parts of the year (winter, spring, early summer). The overflow drip site (JENC2) displays a similar range of variability to the diffuse sites but has only been analyzed two times for $\delta^{18}O$ and $\delta^{2}H$.

A similar disparity is evident from drip water $\delta^{13}C_{DIC}$ values, with fracture fed and overflow sites showing more negative and more variable $\delta^{13}C_{DIC}$ values, compared with the diffuse flow drip sites (Fig. 5A). The $\delta^{13}C_{DIC}$ values of diffuse flow drips vary between -11.5 and -13.6% (VPDB), while fracture fed drips vary between -10.6 and -16.6% (VPDB). Similar to the soil water, fracture fed drips display the lowest $\delta^{13}C_{DIC}$ values during the winter months (Fig. 5A). These winter values are also the closest to the $\delta^{13}C$ of soil water DIC. Drip water DIC displays variable $\Delta^{14}C$ (Table S4); however, diffuse flow drip site BSw4 shows a smaller range of variation in $\Delta^{14}C$ (-72.8 to -83.8%) than the fracture fed drip sites (BSw5, BSw11, BSw12). Site BSw5, the site with the fastest drip rate during the wet season, always displays less negative $\Delta^{14}C$ values than BSw4 (-48.3 to -72.2%) and shows the

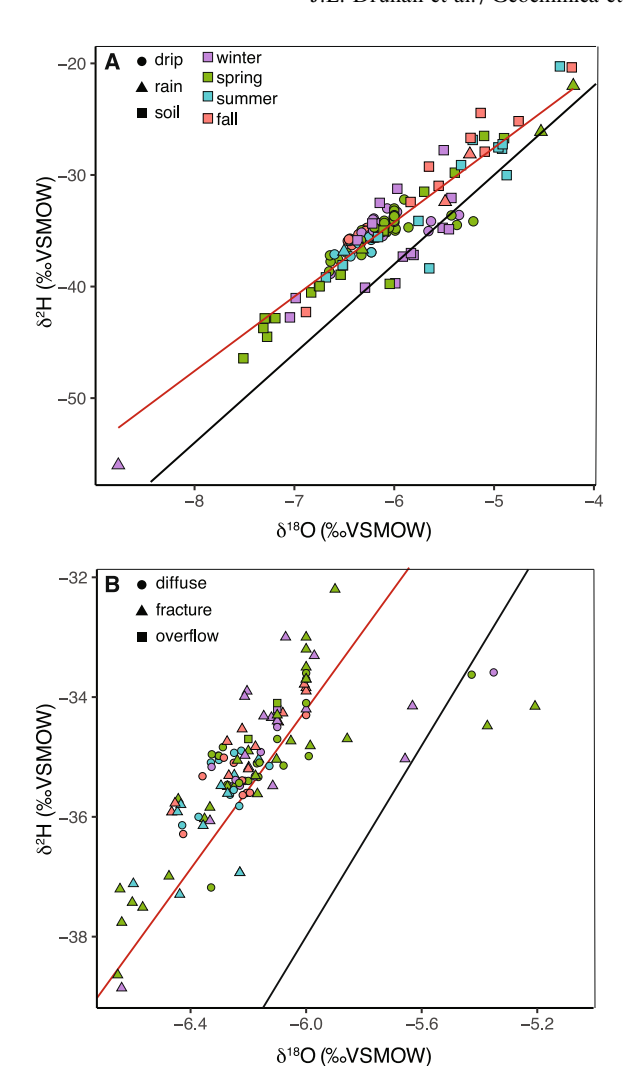


Fig. 6. Drip, rain, and soil water $\delta^{18}O$ and $\delta^{2}H$. (A) All data coded by sample type (drip, rain, soil) and season of collection. (B) Only drip water measurements coded by drip type and season of collection (as in A). Global (black) and calculated local (red) meteoric water lines are shown in both plots. (For interpretation of the references to color in this figure legend, the reader is referred to the web version of this article.)

highest Δ^{14} C values during the fall and winter. Fracture-fed drips BSw11 and BSw12 are the most variable (-48.2 to -96.6‰ and -42.6 to -138.9‰, respectively), at times displaying both higher and lower values than the diffuse flow drip (BSw4).

The average Ca concentration in drip water is 57 ± 13 ppm (1 σ). Diffuse-flow drips range from 38 to 101 ppm, and fracture-fed drips range from 42 to 124 ppm. The cation chemistry of these drip waters is further discussed in the companion paper (Oster et al., this volume).

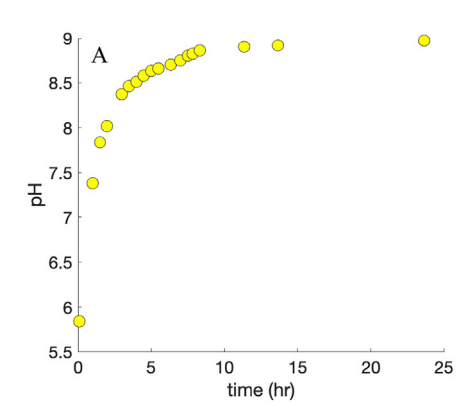
5.2.1. Model constraint: Drip water chemistry and flow rates The concentration of Ca^{2+} is approximately an order of magnitude greater in drip water entering the cave from the overlying host rock (on average 57 \pm 13 ppm (1 σ)) than

that measured at equilibrium in the batch reaction experiments (4 ppm). This observation highlights the important role of the overlying soil and associated organic carbon respiration cycles in maintaining elevated soil pCO₂ and therefore imparting enhanced reactivity to the fluid entering the host rock. This drip water solution chemistry, and the associated δ^{13} C and Δ^{14} C values of DIC in these samples, constitute the principal set of independent observations by which we evaluate the reactive transport modeling results and are not used to constrain model parameters (Table 1)

In contrast to drip water solution chemistry, drip water rates are used to parameterize the model. Diffuse and fracture drips exhibit a wide range of volumetric flow rates, some of which are periodic while others are relatively steady. This is expected to play a role in their relevant geochemical signatures, yet direct conversion of these measurements to fluid flow velocities is complicated by uncertainties associated with the cross-sectional area of overlying karst that contributes to a given drip, the combination of fracture and matrix flow rates, and seasonality of precipitation rates. As a rough estimate, assuming homogeneous drainage rates over a cross-sectional area of 1 m², our observed diffuse fracture drip rates could produce Darcy flux values as low as ~0.01 m/day (5-10 ml/min) and fracture fed drips could be as high as ~0.3 m/day (200 ml/min). Given such uncertainty, we assign fluid drainage rate as a principal parameter in the system (Table 1). The three values of Darcy flux chosen in these simulations are 0.125, 0.250 and 0.500 m/day, which correspond to fluid travel times across the 12 m of limestone in the 1D domain of 67.2, 33.6 and 16.8 days for the prescribed porosity of 70%. We chose not to match the lowest diffusive drip rate velocities from observational estimates, because such extremely low flow rates would result in fluid transit times of over a year and are unlikely to realistically represent drainage through fractured karst. Furthermore, we utilize maximum flow rates greater than those suggested by our drip rate observations to honor the presence of conductive fractures, which could constitute a substantial component of fluxweighted drip waters emerging in the cave. This parameter range is further expanded across many orders of magnitude in fluid velocity in a subsequent analysis (Section 6.4).

5.3. Dissolution experiments and model parameters

Results of the batch limestone dissolution experiment demonstrate a clear rise in pH over the 24-hour period (Fig. 7A), from 5.84 at the initiation of the experiment to a final value slightly greater than 8.9, which stabilizes after approximately 11 hours. Calcium concentrations mirror this trend (Fig. 7B), increasing from effectively non-detectable to a stable value of 4.4 ppm (0.11 mM) over the same period in time. The final dry weight of the recovered limestone sample was 66.907 g, resulting in a net mass lost to solution of 16.8 mg. Assuming a molecular weight of approximately 100 g/mol for the limestone, the change in solid dry weight over the course of the experiment indicates that approximately 0.017 g of limestone dissolved, corresponding to 0.17 mmols of Ca²⁺ or 6.0 ppm (0.15 mM) in solution. This simple mass balance calculation is quite



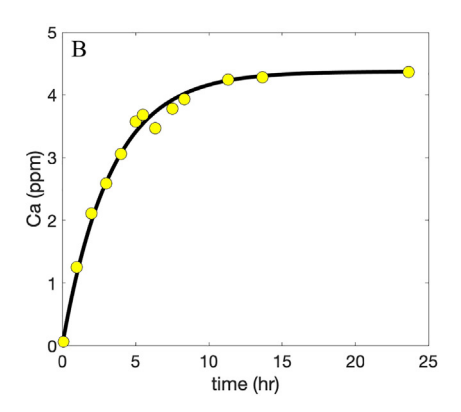


Fig. 7. Fluid chemistry as a function of time during closed system dissolution (i.e. "batch reaction") of a Blue Spring limestone sample. (A) pH evolution over 24 hours of continuous reaction; (B) calcium ion concentration (ppm) over the same period, where the solid line illustrates the simple first-order TST rate expression fit to the data (kinetic rate constant of 1236 mol/m²-hr).

approximate given the error associated with such small changes in weight, as well as the large volume of DI water used, but it is roughly in agreement with the final Ca²⁺ concentration measured in the solution and provides a check of consistency for the batch experimental results.

As a simplified preliminary analysis of these data, we apply a linear transition state theory (TST) rate expression describing the dissolution reaction to verify that data conform to this representation. In comparison to Eq. (1), this formulation simply tracks the concentration of Ca through time and defines Ca_{eq} as the concentration at which point the rate of dissolution is effectively zero. We make no *a priori* assumptions about the value of Ca_{eq} given that the limestone is not pure calcite (Oster et al., this volume):

$$\frac{dCa}{dt} = kA \left(1 - \frac{Ca}{Ca_{eq}} \right) \tag{13}$$

We apply our measured surface area (A) and fit the kinetic rate constant (k) to the timeseries Ca data, as well as the final equilibrated concentration of Ca at the end of the experiment. This simple model very accurately recovers the change in Ca concentration through time (Fig. 7B) for the independently constrained surface area using an equilibrium concentration of 4.4 ppm (0.11 mM) and a kinetic rate constant of 1236 mol/m²-hr (log k = 3.092).

The use of this simple linear TST rate expression incorporates several relevant assumptions. First, the overall reaction is assumed to proceed from an initial state in which the concentration in the fluid is effectively zero to a final state at which an equilibrium value is achieved. This would be analogous to the Blue Spring environment in which rainwater with negligible Ca content percolates rapidly through the soil mantle and reacts quickly with limestone characterized by relatively low surface area. While the approach clearly generates an accurate reproduction of the batch dissolution experiment (Fig. 7B), both the possibility of contemporaneous reprecipitation of secondary carbonate solids and the influences of changing pH, carbonate alkalinity, and exchange between fluid and gas phase CO2 are neglected. Given the potential importance of these factors in karst weathering and speleothem formation, we proceed in developing a more advanced rate expression incorporating these feedbacks and relevant carbonate equilibria using the complete reaction suite implemented in the numerical model (Section 4.2).

The initial conditions of the model include a limestone solid (Eq. (11)) and an initial fluid with a pH of 5.3 and effectively negligible concentrations of cations, dissolved inorganic carbon in equilibrium with the atmosphere and a charge-balanced solution. The starting volume of the limestone is calculated assuming a solid density of 2710 kg/m³ such that for a fluid volume of 1.1 L the overall porosity of the system is 0.978 and the corresponding initial volume fraction of the solid is 0.022, as is reasonable for the physical structure of a batch reactor. The starting specific surface area of the solid is also easily constrained by direct estimate of total surface area and the weight of the block of limestone, resulting in a value of 7.16E-5 cm²/g. However, the experimental design also included a small headspace in order to allow reasonable representation of gas-phase exchange; thus, we construct the model for a fluid saturation of 0.9, meaning that the total volume of the system not occupied by the initial limestone solid is composed of 90% fluid and 10% headspace. In order to maintain the appropriate fluid to solid ratio, the starting volume and surface area of the limestone are then scaled accordingly, resulting in values of 0.0198 volume fraction and 7.93E-5 cm²/g surface area, respectively. The rate constant and equilibrium constant for this particular limestone assemblage (Eq. (2)) are unknown prior to application of the model, and we proceed in the same manner as with the prior simplified TST rate law (Eq. (13)), now including the additional constraint of pH variation and carbonate equilibria (Eqs. (3)–(9)) through time.

5.3.1. Model constraint: Limestone dissolution rate constant and equilibria

The resulting simulations allow simultaneous representation of the change in pH (Fig. 8A) and ${\rm Ca}^{2+}$ concentration (Fig. 8B) over the course of the reaction. The equilibrium constant for this particular limestone assemblage (${\rm K}_{\rm eq}$, Eq. (10)) is constrained to a value of ${\rm 10}^{-9.15}$,

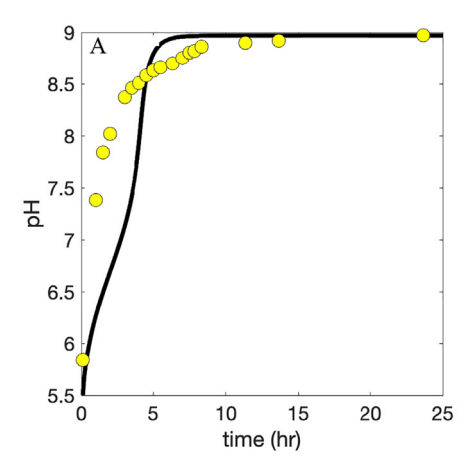
in agreement with the range of values reported in comparable modeling exercises based on natural limestones (e.g. Maher et al., 2004). The corresponding rate constant is then roughly $10^{-5.8}$ mol/m²/yr, which is substantially lower than the value constrained by the simplified model (Eq. (13)) as a result of representing the contribution of total inorganic carbon (and associated equilibria) in the saturation state through time. Relatedly, it is reasonable to expect that the surface area of intact limestone in the Blue Spring system should be much lower than that utilized in the batch reactor, in particular for the cube of limestone cut for this purpose. The cube was extracted from a larger sample and thus offered a fresh, unweathered reactive surface which could be orders of magnitude larger than that regulating fluid-rock interaction in the natural system. In order to represent this influence, we lowered the reactive surface area in the 1D simulations by 1 order of magnitude, resulting in a more appropriate representation on the order of 7.16E-6 cm²/g. This common practice is consistent with many similar model comparisons between laboratory and field conditions (Navarre-Sitchler et al. 2015; Swoboda-Colberg and Drever, 1993; Velbel, 1993; White and Buss, 2014).

An important capacity afforded by this more complete reaction network is the ability to track the saturation state of the system with respect to secondary mineral phases and monitor any precipitates which may begin to form through the course of the reaction. In the dissolution experiment, the starting saturation state is heavily undersaturated with respect to calcite ($\Omega = -11.9$). Based on the stable concentrations achieved at the end of the experiment, the initial fluid is similarly undersaturated with respect to this limestone assemblage ($\Omega = -11.2$). As the reaction proceeds, the system equilibrates with respect to the limestone, ultimately reaching a saturation state that is effectively $\Omega = 0.0$. Under the present experimental conditions, this equilibrated condition is still undersaturated with respect to pure calcite ($\Omega = -0.7$); thus, inclusion of secondary carbonate precipitation is unwarranted under the current batch experiment conditions.

5.4. Base case simulation results

In what follows we begin with a presentation of the simulation conditions described above as a base case set, including the combined treatment of major ion chemistry, radiocarbon, and stable carbon isotope signatures of the drip fluid through the isotope capabilities of the Crunch-Tope software (see Table 2 for a guide to the base case results). From this initial simulation set, we subsequently explore a range of sensitivity tests for each principal parameter in the model. Boundary conditions represent water draining from the base of the soil layer at the top to an open-air cave at the bottom where flow slows down and porosity increases. We apply this model to encapsulate both diffuse and fracture-fed drips, using the variation in flow rate to represent the ensemble of macro- and microstructure surface area of limestone in the porous matrix blocks as well as the fractures that divide them. As described above, three representative flow rates were used in these simulations. In order to make a direct comparison of the drip fluid chemistry between them, each of the three outputs are taken at correspondingly scaled simulation times (1000, 2000, and 4000 days) such that an equal volume of fluid is transported through each simulation. The precipitation of secondary calcite is not considered in these base case simulations, given that saturation with respect to calcite is never reached in the nine sets of flow rate and soil pCO₂. This simplification allows a basic check of the ability of our batch-reaction constrained chemical reaction network to achieve the higher ion concentrations observed in the drip waters for the Blue Spring system relative to those achieved in the batch reactor experiments.

Model results (Fig. 9A) illustrate that the simulated fluid Ca concentrations are principally differentiated according to the assigned upper boundary condition pCO₂. The lowest soil pCO₂ returns an almost negligible increase in Ca concentrations, whereas the highest value causes a rapid increase to as much as 60 ppm at the cave boundary. These concentrations are comparable to measured drip water Ca²⁺ concentrations in the Blue Spring Cathedral Room.



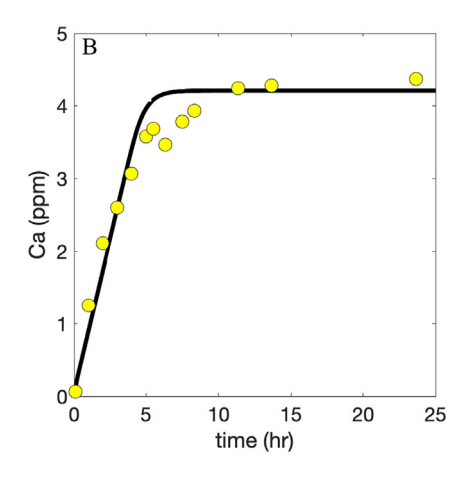


Fig. 8. CrunchFlow numerical simulation (black lines) of (A) pH evolution over 24 hours of continuous reaction; (B) calcium ion concentration (ppm) over the same period (data shown as yellow points). The model simulates limestone dissolution using a first order TST rate expression similar to Eq. (1) but incorporates Eqs. (3)–(9) to additionally constrain carbonate equilibria, pH, saturation state with respect to limestone (and relevant secondary precipitates) through time.

Table 2
A guide to simulation parameter pairs constituting the base case model results from Fig. 9.

Flow rate	Soil pCO2	Graphical representation (Figs. 9–11)
Fast (0.500 m/day)	High (3.0%)	Black solid line
	Mid (1.5%)	Black dotted line
	Low (0.4%)	Black dashed line
Moderate (0.250 m/day)	High (3.0%)	Green solid line
	Mid (1.5%)	Green dotted line
	Low (0.4%)	Green dashed line
Slow (0.125 m/day)	High (3.0%)	Blue solid line
	Mid (1.5%)	Blue dotted line
	Low (0.4%)	Blue dashed line

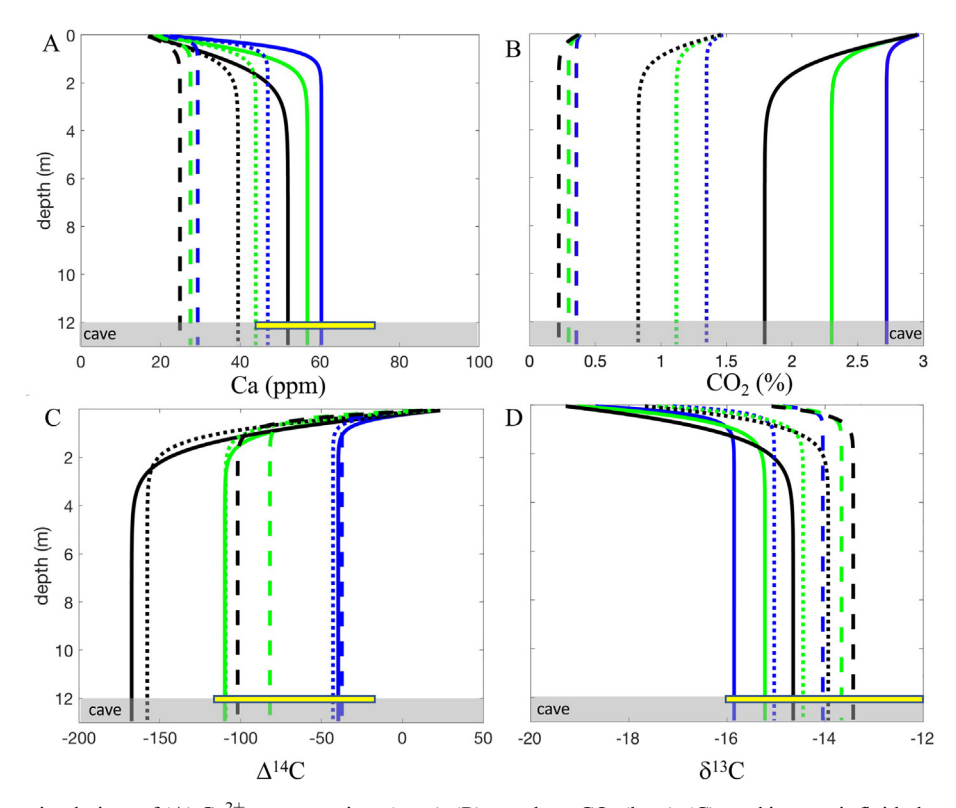


Fig. 9. CrunchTope simulations of (A) Ca^{2+} concentrations (ppm); (B) gas phase CO_2 (bars); (C) total inorganic fluid phase radiocarbon (‰); (D) total inorganic fluid phase $\delta^{13}C$ (‰) across a 13 m depth profile. Nine combinations of three flow rates and three influent pCO₂ values are defined in Table 2. Dilute, acidic fluid infiltrates across the top boundary at fixed flow rates with a chemical composition constrained by soil water monitoring data. The temperature is 13.5 °C. The 1σ range of measured Ca^{2+} concentrations, radiocarbon, and $\delta^{13}C$ DIC values in the measured drip waters are illustrated with yellow bars at 12 m depth (the ceiling of the cave).

A second result of these initial simulations is that the Ca²⁺ concentrations in the fluid exiting the cave system at 12 m depth are only minimally influenced by a fourfold variation in the flow rate. Though secondary to the influence of soil pCO₂, the range of fluid velocities logically returns a higher Ca concentration for a slower flow (blue lines, Fig. 9A) and vice versa. This observation clearly illustrates that for the parameter set thus far constrained by the batch reaction experiment and field measurements, the reactivity of the system is fast relative to transport, and equilibrium between the fluid and limestone is rapidly established as a function of available soil pCO₂ within the upper 1–3 m of the flow

path even for a relatively rapid fluid drainage rate corresponding to a transit time of <20 days for the distance from the base of the soil zone to the cave. Furthermore, we note that the Ca concentrations predicted at 12 m span from much lower, to the median range of concentrations measured in the drip waters (55.2 \pm 14 ppm, for diffuse drips, n = 55, yellow bar in Fig. 9A). In particular, we find reasonable agreement with these measured values using a soil pCO $_2$ of 3% across all three flow rates.

Based on the results of the major ion chemistry, the simulations suggest that we have reasonably constrained the reactivity of the Blue Spring limestone and the boundary conditions unique to the cave system. From the Ca concentration alone, it appears that further slowing fluid flow while maintaining a high soil pCO₂ would allow the concentrations to increase further, matching the higher range of observed values. This is principally a result of the rapid dissolution of the limestone in the shallowest sections of the profile when both soil pCO₂ is high and flow is slow, thus reaching conditions that are closer to equilibrium (Eq. (11)) while maintaining a higher pCO₂ across the domain (Fig. 9B). However, additional independent observational constraints must also be satisfied. In the Blue Spring drip water, the radiocarbon signature (measured Δ^{14} C is typically about -80% for the diffuse drips and -63% for the fracture drips, Fig. 5C, Table S4) must represent some mixing from the dissolution of the Mississippian limestone (effectively radiocarbon dead) and that derived from modern surface inputs (Δ^{14} C of approximately +32%. The corresponding simulated fluid phase inorganic carbon Δ^{14} C (Fig. 9C) again shows reasonable reproduction of the measured values, with a similarly broad range of predicted composition at 12 m. However, this variability is more evenly distributed between soil pCO₂ and fluid flow rate effects. For example, the slowest flow rates return relatively modern Δ^{14} C regardless of the choice of soil pCO₂, whereas at fast flow, these results are much more spread out. It may even appear counterintuitive that the lowest soil pCO2 creates a more modern Δ^{14} C at a fast fluid flow rate, but a check of the corresponding Ca²⁺ results (Fig. 9A) reminds us that this low soil pCO₂ supports minimal limestone dissolution and thus little influence of the radiocarbon-dead endmember. In addition, we observe that only a subset of soil pCO₂ and fluid flow rate combinations satisfy both the observed range of Ca^{2+} and $\Delta^{14}C$ values measured in the Blue Spring drip waters.

These simulations highlight a basic balance between Ca^{2+} and $\Delta^{14}C$ values resulting from mixing between the upper boundary condition (soil water: low Ca²⁺, modern Δ^{14} C) and the dissolution of limestone. However, the behaviors of the two constraints are not identical. In the case of Ca2+, the limestone dissolution process simply increases the concentration to a maximum value dictated by equilibrium and subject to the choice of soil pCO₂. In the case of Δ^{14} C, limestone dissolution lowers the value but in addition the aqueous DIC composition is influenced by the modern Δ^{14} C values of the gas phase CO₂ imposed at the surface and diffusively mixing with the gas in the karst (Eq. (6)). Thus the Δ^{14} C DIC profiles are influenced by more than just two endmembers mixing, as is particularly notable at slow flow rates when time is ample for the DIC and $CO_{2(g)}$ to exchange.

In total, the combined Ca^{2+} and $\Delta^{14}C$ constraints provide a narrow range of acceptable model input parameter combinations. For example, our Ca^{2+} simulations suggest that the lowest soil pCO₂ utilized in our base case set does not produce adequate solute concentrations relative to measured values. In contrast, our $\Delta^{14}C$ simulations suggest that the fastest flow rate chosen in our base case set is sustaining a rapid dissolution rate and thus too negative of a $\Delta^{14}C$ value. Together the results suggest that slow-moderate flow

rates and mid-high soil pCO_2 values produce reasonable agreement with observations.

Finally, we turn to the stable carbon isotope values using the same isotope-enabled CrunchTope framework and the base case simulation described above. The resulting profiles would be a mirror image of the radiocarbon values, reflecting a balance between the surface boundary condition, in this case, the much more positive limestone and the mixing with atmospheric boundary condition pCO₂ across a partially saturated system open to gas diffusion. However, these values show a unique pattern with depth that is distinct from both Ca^{2+} and $\Delta^{14}C$ (Fig. 9D), this time as a result of the additional effects of temperature dependent equilibrium fractionation between and among the DIC species and gas phase CO₂ (Section 4.3). In general, the values predicted at 12 m for the dissolved inorganic carbon are all heavier than they would be without fractionation, and this generates a set of model results that all appear to generally fall within the range of values measured in the cave drip water. Again, as with the radiocarbon, combinations of flow rate and soil pCO2 lead to variations in the $\delta^{13}C$ values. For all flow rates, a higher soil pCO_2 keeps the δ^{13} C value of the drip water from evolving to isotopically heavier values, whereas a lower soil pCO₂ allows the limestone to become more influential (see section 6.2) for further discussion). This somewhat counterintuitive effect is linked to the ease with which gasses can diffuse across the karst and support communication with the upper boundary condition. The corresponding gas phase CO₂ isotope ratios are provided in supplementary information (Fig. S4). Overall, the behavior is consistent with other models of karst dissolution under open versus closed system conditions (Fohlmeister et al., 2011, 2020). Notably, the effects of flow vs. soil pCO₂ overlap in sections of the depth profile, such that any prior calcite precipitation (PCP) formed along the flow path of these systems would reflect a complex signal of transport and transformation that would be challenging to disentangle without the aid of such a discretized simulation framework. The potential effects of PCP and other parameter sensitivities are discussed in further detail below (Sections 6.3 and 6.4).

6. DISCUSSION

6.1. Observations of carbon isotope systematics in the modern cave

6.1.1. Drip Water

The $\delta^{13}C$ and $\Delta^{14}C$ values of Blue Spring drip water DIC suggest variable modification of soil water signatures during transit of the water from the surface to the cave. The longer records from supposed fracture-fed drips (BSw5, BSw11, BSw12) show higher variability in $\delta^{13}C_{DIC}$ than supposed diffuse flow drips (BSw4 and BSw10) and consistently low $\delta^{13}C_{DIC}$ during the winter months. Lower winter $\delta^{13}C_{DIC}$ values occur during intervals when effective rainfall is high (Fig. 5A) and the $\delta^{13}C_{DIC}$ value of deep soil water is also lower (Fig. 5B). Generally, local minima in drip water $\delta^{13}C_{DIC}$ values appear to lag local maxima in effective rainfall by approximately one month (Fig. 5A).

The limited variability apparent in diffuse flow drip sites displays a less consistent pattern with effective rainfall, showing relatively low values only during the winters of 2013/14 and 2014/15. The variable Δ^{14} C values of the fracture fed drip waters indicate that the amount of host rock dissolution and gas exchange in the karst likely does vary throughout the year along the flow paths leading to these drip sites. The more consistent $\delta^{13}C_{DIC}$ and $\Delta^{14}C$ for diffuse drip site BSw4 reinforces a consistent host rock contribution to DIC in drip water from this type of flow path. This supports observations of a more constant drip rate and less variable δ^{18} O (Fig. 6) at both BSw4 and BSw10, indicating these drips reflect a comparatively well-mixed reservoir of water in the host rock. Although there is no clear relationship between Δ^{14} C and δ^{13} C_{DIC} values for the fracture fed drip sites overall, taken site by site, higher $\delta^{13}C_{DIC}$ value is often associated with lower $\Delta^{14}C$ (Fig. S3), which is consistent with the results of our model base case scenarios (Fig. 9c and d). However, observation of lower drip water δ¹³C_{DIC} values during winter when we measured faster flow rates and lower soil pCO2 is apparently inconsistent with our base case modeling results, where slower flow and higher pCO₂ are associated with lower $\delta^{13}C_{DIC}$ values due to enhanced gas exchange with the soil zone. These observations of drip water $\delta^{13}C_{DIC}$ values may be suggestive of the influence of degassing of CO2 on fracture fed drips, as periods of higher infiltration would be consistent with shorter drip intervals and therefore less degassing and PCP at the drip site and lower $\delta^{13}C_{DIC}$ (Fohlmeister et al., 2020). However, we note that our measurements of soil waters also suggest that the δ^{13} C values of deep soil water DIC are also more negative in the winter months (Fig. 5b), perhaps due to seasonal, temperature dependent changes in soil respiration (e.g. Breecker et al., 2012a). This indicates that seasonal variations in the δ^{13} C value of infiltrating soil water may also contribute to this variability. Below, we employ the RTM, utilizing the balance between Ca^{2+} and $\Delta^{14}C$ to disentangle the influence of host rock dissolution and ultimately degassing of CO2 on drip water carbon isotope values.

6.1.2. Cave Air

The Blue Spring Cave system shows several characteristics that are consistent with commonly observed conditions in modern temperate cave environments. The higher cave air pCO₂ during the summer months, lower pCO₂ during the winter months, and increasing pCO₂ with distance from the cave entrance is consistent with seasonal, air density driven ventilation of the cave system (e.g. Banner et al., 2007; Oster et al., 2012, Kowalczk and Froelich., 2010; Frisia et al., 2011; Mattey et al., 2016) (Fig. 3). Variability in the δ^{13} C values of cave air (-11 to -21‰) suggests CO₂ is derived from mixing between surface air and gas from the soil zone and deeper within the host rock (Fig. 4A), similar to observations in Grotta di Ernesto, Italy (Frisia et al., 2011).

Lower cave air δ^{13} C values during the summer months, when pCO₂ is high, are consistent with increased contribution of respired carbon from the soil or deeper carbon sources within the fractures in the host rock. The one radio-

carbon measurement of the cave air CO_2 ($\Delta^{14}C = 24.2\%$), falls between the mean soil CO₂ (3.8%) and soil water DIC (37.2%). All of these components of the system (soil gas, soil water, cave air) show positive Δ^{14} C values, reflecting modern ages and the presence of bomb-derived radiocarbon (i.e. fixed from the atmosphere since 1950). Consistent with observations from other cave systems (Wong and Banner, 2010; Knierim et al., 2015; Bergel et al., 2017), the modern radiocarbon age of the cave air argues against degassing of CO₂ from drip water as a major source of cave air CO₂ because the drip water DIC displays much lower Δ^{14} C values that are reflective of dissolution of the radiocarbon dead host limestone. Likewise, the modern radiocarbon age suggests minimal influence of old organic carbon sources in the host rock zone on cave air CO₂, in contrast to Texas caves that display cave air CO₂ radiocarbon that suggest that decaying (pre-modern) organic carbon is a substantial contributor to cave air CO2 (Bergel et al., 2017). Thus, both radiocarbon and δ^{13} C values of cave air from Blue Spring Cave reflect carbon inputs from soil or deeper CO₂ sourced organic matter, plant root respiration and/or surface air CO₂.

6.2. Reactive transport model behavior and comparison to other modeling approaches

6.2.1. Soil carbon models

Comparison of the base case set of simulations (Fig. 9) to our drip water data from Blue Spring highlights a key balance between the necessity to generate enough solubilization of limestone to produce sufficiently high Ca²⁺ concentrations (Fig. 9A), while simultaneously maintaining reasonably modern radiocarbon DIC (Fig. 9C). This balance cannot be achieved in a closed system. Rather, we find that it is necessary to maintain open connectivity between the limestone and the upper boundary condition through a gas diffusion coefficient that is essentially equivalent to the free air diffusivity of CO₂. Limiting this rapid communication to any lower value of diffusivity negates the balance between sufficient reactivity and radiocarbon modern DIC (Supplementary Information Fig. S5). We choose to utilize this approach rather than introduce an additional unconstrained gas phase flow velocity parameter, but we do not suggest that gas advection may be ruled out in this or similar systems. We note that this observation is also consistent with theoretical models of CO₂ transport in karst systems (Covington, 2016), though here we are able to accomplish sufficient rates of communication between the upper boundary condition and the karst interior through a free air diffusivity rather than via gas phase advection. Such sustained reactivity in an open system is somewhat comparable to the soil carbon models discussed in Section 4.1 (Eq. (2)), where a balance between a CO₂ production term and CO₂ diffusivity describes the steady state gas phase profile as a function of depth. Indeed, many seminal papers in the soil carbon literature model δ^{13} C profiles (Cerling, 1984; Quade et al., 1989; Cerling et al., 1991) and radiocarbon profiles (Wang et al., 1993) that appear comparable to those illustrated in Fig. 9C and D. In these soil carbon models, an atmospheric CO2 endmember mixes

with a soil organic matter endmember. In the present context, we are essentially mixing a soil pCO₂ endmember with a limestone endmember.

From this basis it may seem reasonable to apply Eq. (2) to the present system and solve the attendant equilibria to obtain carbon speciation and isotope ratios. This would present a simpler alternative to construction of a multicomponent RTM. However, the use of Eq. (2) is predicated on the fact that soil carbon respiration (R_s) is a source of CO_2 , thus allowing the resulting CO₂ profile to mix two distinct endmember isotopic compositions. The CO₂ profiles produced in Fig. 9B remind us that the solubilization of limestone consumes acidity (Eq. (11)); and thus the pCO₂ within the karst decreases relative to the soil boundary condition (in the absence of any additional inputs, considered further in Section 6.4). Simply making the production term in Eq. (2) negative to create a sink of CO₂ could produce such a pCO₂ profile but removes the capability to mix together two sources of carbon with unique isotope ratios (e.g. atmospheric and organic matter). Therefore, the reactive transport simulation is necessary to provide the complete simulation of Ca²⁺, pCO₂, δ¹³C value and radiocarbon of DIC, in that it provides the means to simulate a reaction that consumes acid (Eq. (11)) and thus lowers pCO₂ (eq (6)), while simultaneously allowing the solubilization of limestone to introduce carbon of unique isotope composition into the fluid and gas phases (Eqs. (3)–(9) and (11)).

6.2.2. Carbonate equilibria models

A more common modeling approach applied to cave drip waters is to essentially lump all effects of transport into the extent to which the system is 'closed' (i.e. pCO₂ is a variable) vs. the extent to which it is 'open' (i.e. pCO₂ is fixed), as described in Section 4.1. The model then tracks the evolution of DIC, δ^{13} C and radiocarbon values as the fluid transitions from equilibrium with this initial condition to one that is equilibrated with a carbonate mineral (Hendy, 1971). Systems that are neither strictly open or closed have been approximated with this modeling approach by allowing the fluid to advance some percentage of the way towards equilibration with carbonate under strictly open conditions, and then switching to closed conditions for the remainder of the solution (Fohlmeister et al. 2011). This framework provides an interesting opportunity to contextualize the behavior of our reactive transport simulations. Our nine base case simulations utilize three values of soil pCO₂, which allow us to populate a log-log plot of HCO₃ vs. pCO₂ as the fluids approach equilibrium with respect to the limestone (Fig. 10A). Several notable observations appear. First, the three fluid flow rates utilized for each soil pCO₂ value produce three distinct results in the approach to carbonate equilibration. Following Hendy (1971), greater curvature indicates a system that is closer to closed-endmember behavior. In our models, this corresponds to the fastest fluid flow rate. Second, none of the models completely achieve equilibrium with respect to the limestone, despite the fact that they appear equilibrated in Fig. 9. This is due to the fact that the reaction rate (Eq. (13)) describing the solubilization of the limestone slows down drastically in the approach to equilibrium, yet

the fluid transits the system fast enough that it does not completely cease, reminding us that a balance in timescales exists between how quickly fluid can react with the solid phase and how quickly it can drain from the surface into the cave. The key point for our purpose is to recognize that all nine solutions achieve essentially equivalent proximity to equilibrium, thus allowing us to compare the compositions of these fluids at the same location in the model domain at 12 m where the fluid reaches the cave ceiling.

Upon this basis, we turn to the carbon isotopes. Radiocarbon (Fig. 10B) and δ^{13} C (Fig. 10C) are illustrated as a function of pCO₂ following the approach of Fohlmeister et al. (2011). Once again, the transition from our modeled upper boundary condition to drip water compositions creates three unique trajectories for each soil pCO2 value due to the difference in fluid drainage rates. We delineate the radiocarbon and δ^{13} C values of the fluid at the cave ceiling for these three flow rates, resulting in contours that are differentiated by the extent to which the system is behaving as open vs. closed. Unlike Fohlmeister et al. (2011), we do not assign specific ratios of open/closed behavior to these contours, because we do not choose such a ratio in the process of solving the model. Where Fohlmeister et al. (2011) would solve a purely open system for some percentage of the approach to carbonate equilibria and then transition to a closed system, here the behavior emerges as a result of the transit times of fluid and gas through the system for a given soil pCO₂. Essentially, our model produces these open/closed ratios as a variable that may change even along the flow path of a given simulation. None of our model simulations are purely open or closed at any point in the domain.

The reactive transport modeling approach applied here highlights a key point with regard to the treatment of cave systems as some combination of open and closed. These terms encapsulate multiple transport pathways. Commonly, an open system is thought of as one that is able to maintain a pCO₂ equivalent to the overlying boundary condition. This can occur if the gas phase is able to easily move through the karst due to either a high rate of diffusivity or advective flow. However, it is also tied to the ability of fluid to drain through the system. For the same soil pCO₂ and the same gas phase diffusion coefficient, unique fluid drainage rates produce unique pCO2 profiles (Fig. 9B). This results from the movement of a reactive fluid actively interacting with limestone to consume acid and lower pCO₂ deeper in the domain for a faster flow rate. If fluid moves fast enough relative to the rate at which pCO₂ can diffuse (or advect), this fluid essentially isolates itself from the upper boundary condition, thus leading to behavior that is closer to a closed system.

6.3. The potential for prior calcite precipitation

From these results, it is evident that the radiocarbon content of fluid exiting at the cave ceiling reflects a mixture of sources, and thus is not a metric for absolute age or travel time. If we were to omit stable isotope fractionation and only include the $\delta^{13}C$ value of the upper soil boundary condition, the $\delta^{13}C$ value of the dissolving limestone, and the

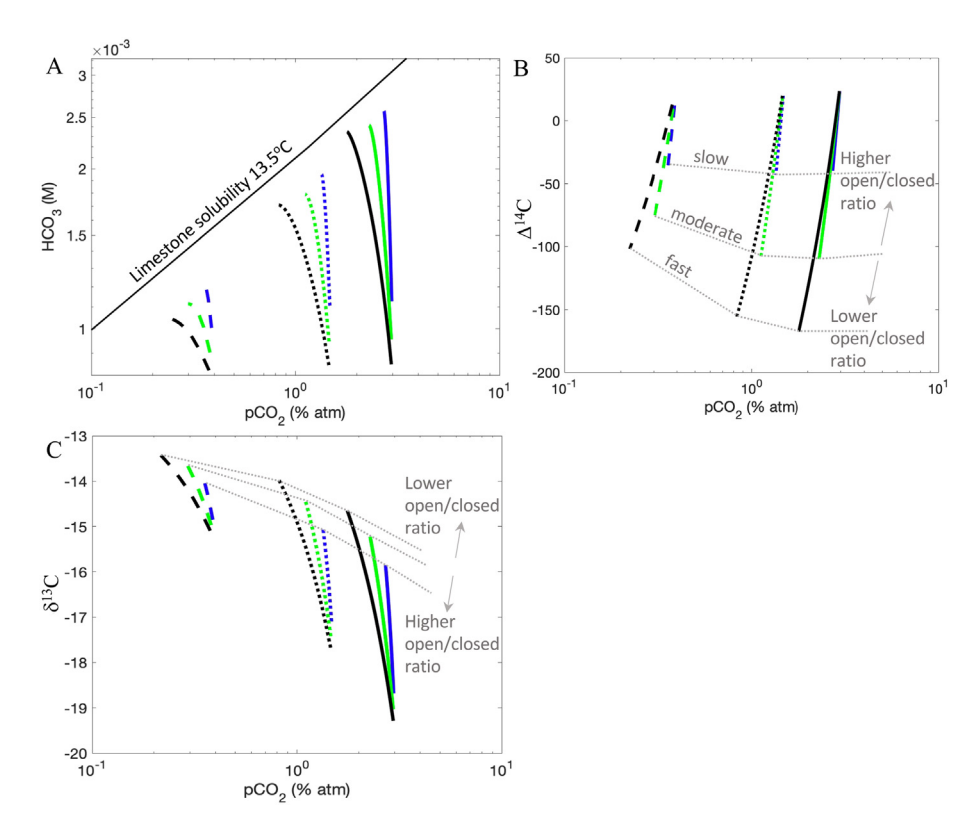


Fig. 10. CrunchTope simulations comparing (A) speciated concentration of HCO_3 (M) (B) radiocarbon of DIC (‰) and (C) $\delta^{13}C$ of DIC (‰) all vs. pCO_2 (% atm). Nine combinations of three flow rates and three influent pCO_2 values are defined in Table 2. In all simulations, the evolution of parameter space largely occurs over the upper ~4 m of the model domain (Fig. 9). Panel A provides a reference point for the solubility of this limestone, as constrained by the batch reaction experiments, starting from the same initial conditions as the 1D model and allowing the system to achieve equilibrium in the absence of flow. The radiocarbon (B) and $\delta^{13}C$ (C) of DIC in the drip water emerging in the cave at 12 m depth are illustrated for each of the three flow rates by dashed grey lines. The relative ratio of 'open' vs. 'closed' system behavior is labeled following the notation of Fohlmeister et al. (2011). The precise value of this open/closed ratio is not defined as in Fohlmeister et al. (2011), because in our model does not mix a ratio of pure 'open' and pure 'closed' systems. Rather, the relative "open vs. closed" behavior of this model is a variable that emerges as a result of the choice of fluid drainage rate and soil pCO₂.

solubilization or exchange with gas phase CO2 diffusing across the domain, the δ^{13} C value would mirror the behavior of the radiocarbon. However, mass-dependent fractionation strongly influences the distribution of δ^{13} C such that these values do not mimic Δ^{14} C data. Allowing this equilibrium fractionation elevates all of the δ^{13} C DIC in the fluid entering the cave to values between -15.9 and -13.4%, within the range measured in the drip waters collected from the Blue Spring Cathedral Room (Figs. 5 and 9D). The δ^{13} C and Δ^{14} C solution space afforded by the nine pairs of flow rate and soil pCO₂ defining our base case overlaps with a subset of measured values in drip water collected in Blue Spring Cave (Fig. 11). This agreement suggests that in general, these drip waters are not subject to extensive PCP within the host rock above the cave ceiling prior to collection. Notably, a substantial PCP effect would limit the maximum Ca²⁺ concentrations achievable in these fluids (Fig. 9A), which would perpetuate undersaturation with respect to the limestone, thus pulling more radiocarbon depleted DIC into solution. Neither a decrease in Ca²⁺ or Δ^{14} C of DIC are supported by this data – model comparison. However, a subset of drip water DIC measurements does suggest a slightly more positive δ^{13} C ratio than the

model solution space (Figs. 9D, 11). This subset of data, in conjunction with evident speleothem growth within the cave, suggests minor amounts of PCP along some flow paths without substantially influencing the major cation or radiocarbon values. Additionally, the occurrence of more negative drip water δ^{13} C during intervals of higher net rainfall that is observed at fracture-fed drips (Fig. 3A) is consistent with reduced drip water degassing and PCP during times of shorter drip interval (and faster drip rate) (e.g. Fohlmeister et al., 2020). We reiterate that none of the nine base case simulations achieved fluid compositions that crossed the threshold for calcite solubility, such that any degassing and PCP affecting these measurements is likely to have occurred at the ceiling of the cave where the fluid is exposed to the open-air space. These effects are explored further in the companion paper using trace element cation ratios (Oster et al., this volume).

6.4. Parameter sensitivity

Based on the results of our data – model comparison, we consider the base case simulations of fluid entering the cave from the overlying host rock and mixing with the cave air to

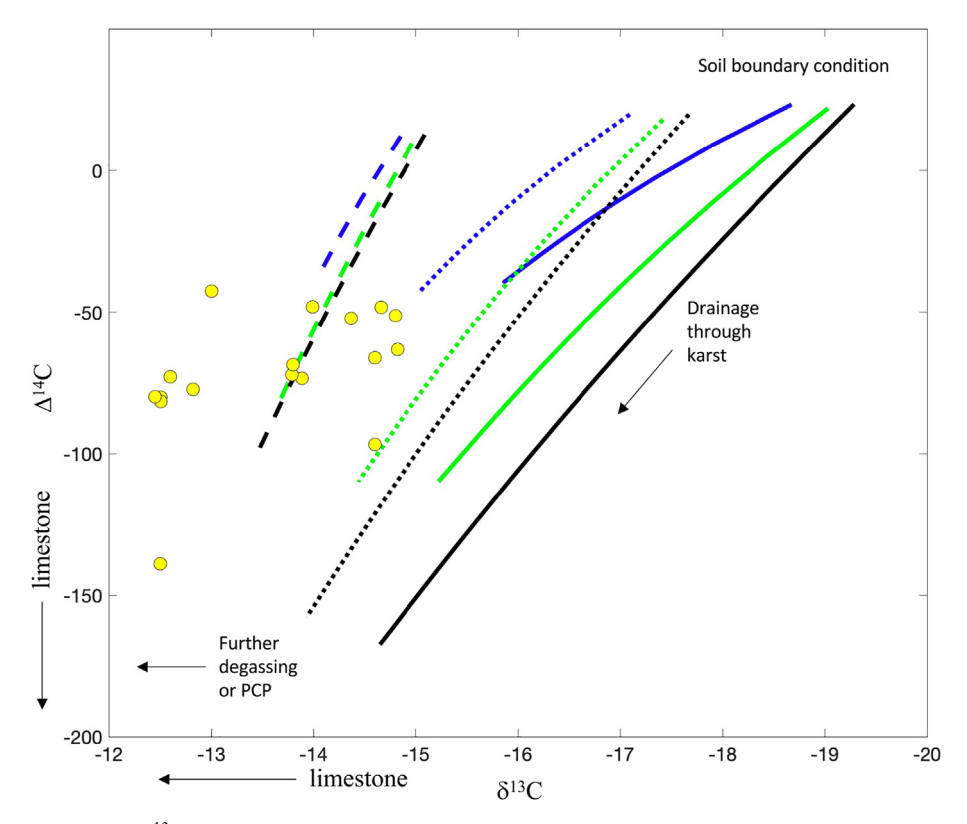


Fig. 11. CrunchTope-simulated $\delta^{13}C$ vs. radiocarbon in DIC of the fluid entering the cave over the last 1 m of the domain. Nine combinations of three flow rates and three influent pCO₂ values are defined in Table 2. The upper boundary condition of each simulation plots to the upper right. DIC isotope ratios evolve towards the composition of the limestone (lower left), terminating in the modeled isotopic composition of drip water entering the cave. The $\delta^{13}C$ axis is plotted from high to low, consistent with the presentation in Fohlmeister et al. (2011). A negative correlation between $\delta^{13}C$ and radiocarbon is generally observed, where the slowest flow rate returns values that are closest to the surface signatures, while faster flow with higher soil pCO₂ conversely creates extensive reaction with the epikarst, leading to more positive $\delta^{13}C$ and more negative radiocarbon. Measured values from drip water collected in the Cathedral Room in the Blue Spring Cave are illustrated in yellow circles, and the trajectory of influence due to further degassing or prior calcite precipitation (PCP) is indicated.

reflect a reasonable process-based description of the Blue Spring system (Figs. 9 and 11). From this basis, we are now poised to explore the sensitivity of the model results to a variety of effects beyond the conditions of this particular cave system. Using the base case as a starting point, we consider the effects of fluid flow rate, soil pCO₂, porosity, and fluid saturation, additional pCO₂ sources and the effects of the cave air on the resulting simulated evolution of solutes and isotope signatures.

Beginning with flow rate and surface pCO₂, the model simulations are expanded to 4 orders of magnitude range fluid velocity (Fig. 12). This choice of fluid velocity parameter space is a result of the behavior of the model developed for the present application. Specifically, for the reactivity constrained by our batch reactions for the Blue Spring limestone, the pCO₂ and fluid composition of the overlying soil, and the 12 m thickness of limestone, we find that a 4 orders of magnitude variation in fluid velocity encompassing the values tested in the earlier models produce the entirety of possible variation in cave drip water radiocarbon values (discussed further below). Further, a 4 orders of magnitude variation in drip rates have been reported previously even within a single cave system (Miorandi et al., 2010). We emphasize that application of the present model to a differ-

ent cave system, featuring unique water-rock reactivity, environmental conditions and characteristic length scales would require distinct analysis, but the overall relationships between fluid velocity and drip water chemistry should remain comparable. The results continue to be taken at equivalent fluid pore volumes, such that fast flow rates are simulated for a short period of time and slow flow rates are simulated for an appropriately scaled longer period of time. Each simulation exposes the same amount of moving fluid to the limestone. The behavior of the Ca²⁺ major ion (Fig. 12A) illustrates a strong dependence on soil pCO₂ at slow fluid flow rates, creating the highest Ca²⁺ under high soil pCO₂ conditions. This dependence is lost as fluid velocity accelerates. Ultimately, under conditions where the fluid transits the limestone in <10 hours, the Ca²⁺ concentration is uniformly low regardless of soil pCO2. The corresponding radiocarbon DIC values similarly lose sensitivity to soil pCO₂ at the fastest flow rates (Fig. 12B). Unlike Ca²⁺, radiocarbon values are also equivalent for all choices of soil pCO₂ at the very slowest flow rates. Under both endmember conditions, the Δ^{14} C values are effectively modern, highlighting the effects of rapid transit due to fast flow and equilibration between the DIC and CO_{2(g)} phases in communication with the upper boundary condition at slow

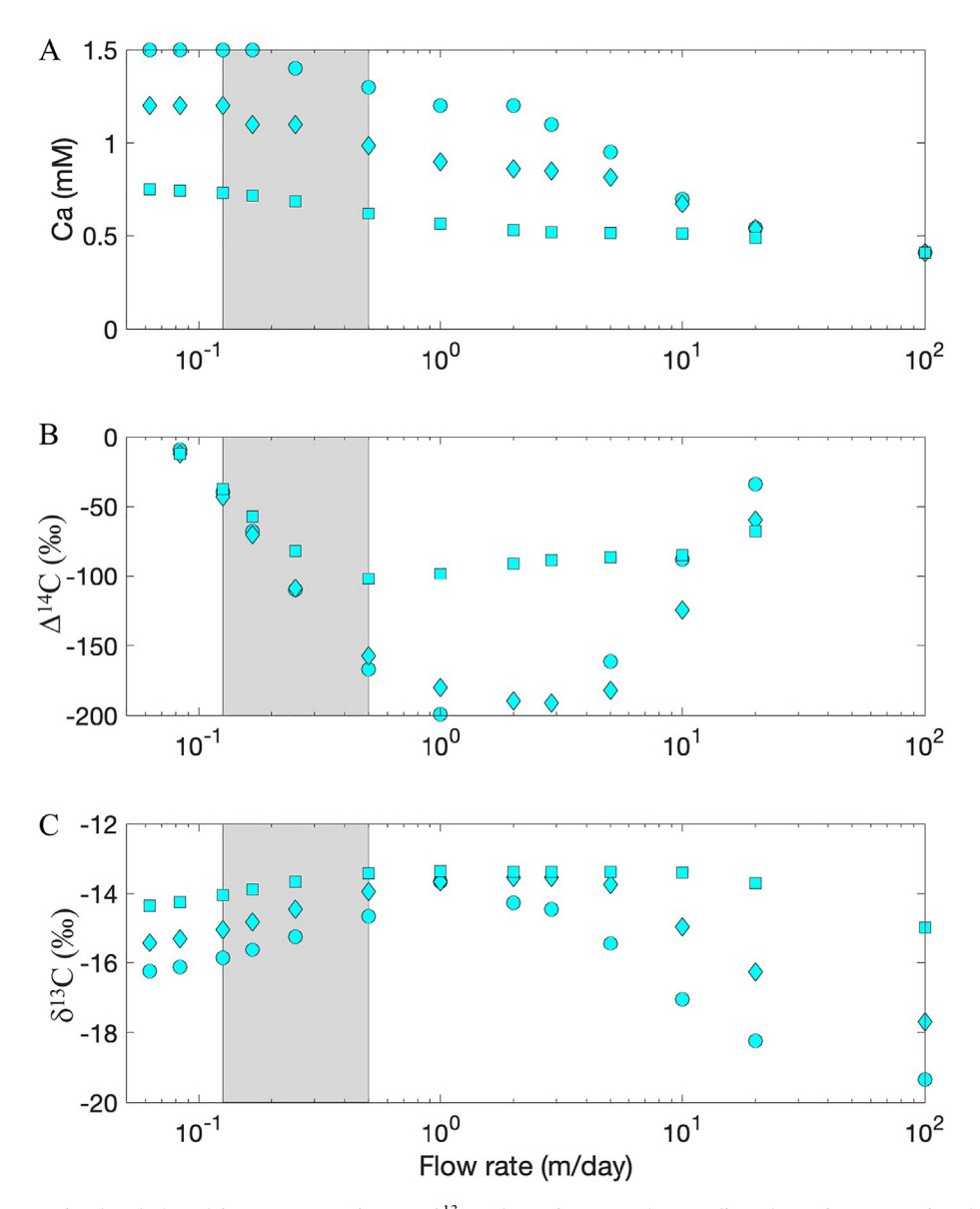


Fig. 12. CrunchTope-simulated (A) calcium concentration; (B) δ^{13} C values of DIC; and (C) radiocarbon of DIC entering the top of the cave (12 m) in our discretized domain over a broad range of fluid flow rates. Results are shown for the three influent pCO₂ values, high (circles), middle (diamonds), and low (squares). Grey shading indicates the range of fluid flow rates used in the base case simulations (Fig. 9). Stable isotope ratios are subject to temperature-dependent fractionation among DIC species and gas phase CO₂. For simplicity, radiocarbon values are taken immediately upon entry to the cave, and further mixing with a modern cave air boundary condition is not considered (Fig. 11). All simulations are run such that the same volume of pore water is transported through the domain for each flow rate. This results in a range of simulation times from 5 to 8000 days.

flow. Only in an intermediate range of flow rates do the $\Delta^{14}C$ of DIC values in fluids reaching the cave reflect sensitivity to the choice of soil pCO₂ and thus the reactive potential of the fluid. Under these intermediate conditions, a lower soil pCO₂ leads to less limestone dissolution and thus a more modern radiocarbon value. Finally, the $\delta^{13}C$ DIC values incorporate the additional effect of temperature dependent fractionation and offer a very different pattern of behavior (Fig. 12C). Here, intermediate flow rates return effectively comparable $\delta^{13}C$ ratios for any choice of soil pCO₂. Both slow and fast fluid velocities support increased sensitivity to the choice of soil pCO₂ and thus the initial

reactivity of the fluid. Across the entire range of flow rates, the lowest soil pCO₂ content creates the most positive δ^{13} C values, which are furthest from the -20% δ^{13} C of the soil pCO₂ boundary condition.

In Blue Spring drip water $\delta^{13}C_{DIC}$, we observe the lowest values during winter and spring (Fig. 5), the seasons when soil pCO₂ is the lowest (Fig. 3). In contrast, the model indicates a decreased $\delta^{13}C_{DIC}$ value at higher soil pCO₂ for a given flow rate (Fig. 12C). Several factors should be considered in this comparison. First, the winter months at Blue Spring are associated with a combination of higher flow rates and lower soil pCO₂, as opposed to summer months

where soil pCO₂ is higher and average fluid drainage rates are nominally lower. The model predicts that high flow rates and low soil pCO₂ would produce drip water $\delta^{13}C_{DIC}$ values of approximately -13.4%, whereas low flow rates and high soil pCO₂ would create more negative values of approximately -15.8%. However, individual precipitation events or periods of drought may push the flow rate of fluid at a given drip site to values outside of the base case scenario. Looking across the entirety of the simulation space (Fig. 12C), evidently, even a moderate expansion in the range of fluid flow rates can support conditions in which a high soil pCO₂ and fast flow achieve a $\delta^{13}C_{DIC}$ value that is more positive than a low soil pCO₂ at slow flow. Second, we note that a correction for differences in soil temperature between summer and winter does not alleviate this issue. Forcing the upper boundary condition to a temperature of 4 °C while maintaining the cave interior at 13.5 °C creates a slightly larger disparity between fast flow, low soil pCO_2 ($\delta^{13}C_{DIC} = -13.1\%$) and slow flow, high soil pCO_2 (-15.9%), thus failing to resolve the discrepancy. Third, our measurements of soil CO2 are somewhat limited, as are drip water samples at the height of the summer season when drip rates become very slow. Thus, identifying a consistent influence of soil pCO₂ on drip water $\delta^{13}C_{DIC}$ value may be premature given the available data. For example, at a given soil pCO₂ value, the low $\delta^{13}C_{DIC}$ values at fracture flow sites during the winter months could be interpreted to reflect very fast flow rates during times when rainfall is high and fluid velocities exceed the boundaries of the base case simulation set (Figs. 5 and 12). Further, our observations suggest modification of drip water δ^{13} -C_{DIC} values by degassing of CO₂ on the cave ceiling (Fig. 11) may be necessary to produce the highest measured values, which tend to occur in the summer months (Fig. 5) when soil pCO₂ is high, flow is slow, and therefore drip interval on the cave ceiling is long. Thus, degassing of CO₂ on the cave ceiling may provide an additional influence that helps to explain the observed seasonality in our data set.

Next, we turn to the choice of a 70% porosity and 20% fluid saturation as a representation of the ensemble of easily drained fractures and porous limestone. In general, these values are strongly skewed towards an open, unsaturated system where gases freely diffuse across the entirety of the host rock and easily communicate with the overlying soil boundary condition. Under such conditions, it is difficult to imagine that the fluid content of the limestone would ever reach bulk values (encapsulating both porous blocks and fractures) that approach saturation. Assuming that fluid saturation remains well below 100%, the modeled Ca concentration and carbon isotope ratios are effectively insensitive to the choice of this parameter. However, decreasing the porosity of the system (and correspondingly the tortuosity-corrected gas phase diffusion coefficient) has a strong impact on the model results. Simply lowering the gas phase diffusivity to 0.01 cm/s² as is typically implemented in partially saturated soils and porous media (Steefel and Maher, 2009; Lawrence et al. 2014), we find that the extent to which Ca²⁺ can be dissolved into solution is impeded (Fig. S5A). In addition, radiocarbon DIC values

are universally much lower than those in the base case simulation. These factors are both linked to the difficulty with which soil pCO₂ can diffuse into the host rock as the limestone weathering reaction proceeds. This both limits the extent of limestone dissolution (lower Ca²⁺) and the extent to which radiocarbon DIC can exchange with a modern soil gas pCO₂ (lower Δ^{14} C of DIC). Thus, any effect which limits communication between the host rock and the overlying soil layer leads to a highly restricted balance in which the simulation cannot simultaneously produce enough dissolved Ca^{2+} and a sufficiently modern $\Delta^{14}C$ of DIC. The result is that our model requires the combination of a high porosity, low water saturation and free air diffusivity of $CO_{2(g)}$ in order to produce results that overlap with the range of measured values in the Blue Spring drip water. This sensitivity suggests that cave systems which are less communicative with the overlying atmospheric boundary condition than Blue Spring may exhibit a seemly counterintuitive combination of lower Ca²⁺ concentrations and drip water radiocarbon signatures that are more strongly influenced by the limestone. Such an environment may be found in the tropics. For example, Griffiths et al., (2012) found increased contribution of the host rock to the dead carbon fraction of an Indonesian stalagmite during intervals when heavy monsoon rainfall and waterlogging would have limited contact between the soil gas and host rock. Finally, the corresponding δ^{13} C of DIC fall into an even tighter range of values than the base case simulation, principally as a result of the narrower range of pCO₂ distributions across the host rock.

These sensitivity exercises highlight the tight coupling between the gas phase and dissolved inorganic carbon species isotope ratios. Ease of communication of CO_{2(g)} between the host rock and soil boundary condition maintains a more modern radiocarbon DIC, and also produces a broader range of δ^{13} C DIC values in the drip water reaching 12 m in our simulations. This suggests that below 12 m, the presence of the open air in the cave should also influence these values. In the base case simulations, this effect was largely omitted through the use of a Neuman boundary condition, which pins the gradient rather than an absolute value of concentration or partial pressure. The benefit in this construction is that it does not force the cave air to a single value of pCO₂ or associated carbon isotope ratios, eliminating the potential for diffusive gradients which extend upward into the overlying limestone. However, the drawback is that the cave air conditions are entirely dictated by the geochemistry and transport processes that occur in the overlying karst, without any representation of lateral communication between the cave entrance and interior. In reality, the interior of the cave is a mixture between these effects (Fig. 4A). Therefore, the real system is something of a mixture between the two choices of boundary condition afforded in this 1D RTM simulation. To consider these effects, we reran the base case simulations with a lower Dirichlet boundary condition such that concentrations are pinned at the base of the domain, 1 m below the cave ceiling. Again, across the last 1 m of the domain, fluid is subject to a much slower flow rate without any exposure to limestone, such that the fluid phase Ca²

concentrations are not strongly impacted by this lower boundary condition (Fig. S6A). The choice of cave pCO₂ is thus the most notable constraint, and we illustrate one result using a relatively low value of 0.8% comparable to Blue Spring Cathedral Room values in winter (Fig. 3). This fixed cave air boundary strongly influences the distribution of pCO₂ throughout the host rock, which is now subject to two gas phase boundary conditions with a capacity to rapidly diffuse between them (Fig. S6B). Clearly, fixing a pinned value of pCO₂ in the cave is not an ideal way of exploring the parameter space produced by fluid draining through this partially saturated system; thus, this fixed value was not utilized in the base case simulations. However, its use here allows us to correspondingly fix both the Δ^{14} C and δ^{13} C value of the cave air, and we choose values representing the relatively modern cave air pCO₂ observed in Blue Spring measurements (Section 5.1) with an average Cathedral Room δ^{13} C pCO₂ value of -21.8% (Fig. 4).

These conditions create simulated fluid DIC isotope ratios that are strongly influenced by the pCO2 and isotope ratios fixed at the bottom Dirichlet boundary condition representing the cave air (Fig. S6). The radiocarbon and δ^{13} C in the DIC exiting the host rock as drip water on the cave ceiling rapidly equilibrate with the surrounding cave air. This causes the Δ^{14} C DIC values to shift to more modern ratios due to the relatively modern cave air pCO₂. The corresponding δ^{13} C value of DIC remains in a range of -15 to -13% despite the fact that the cave air boundary condition pCO₂ value is set to -21.8%, again as a result of the equilibrium fractionation between DIC predominantly existing as HCO_3^- and the cave air $CO_{2(g)}$. However, the δ^{13} C values all shift to more positive ratios than their counterparts in the base case simulation (Fig. 9D), thus suggesting that the more positive measured δ^{13} C value of DIC in some cave drip waters could also reflect partial equilibration with the cave air in addition to degassing of CO₂ with attendant stable isotope fractionation (Fig. 11). A second observation from this revised boundary condition is that under conditions where cave air pCO₂ is higher than the pCO₂ in the overlying karst (Fig. S6B), a strong gradient can draw cave air up into the cave ceiling. This supply of elevated pCO₂ contributes reactivity to the fluid phase and promotes further dissolution of limestone, as noted in both increased Ca²⁺ (Fig. S6A) and decreasing radiocarbon (Fig. S6C) when the upper soil boundary pCO₂ is low.

Finally, we turn to an analysis of the effects of a deep source of modern CO_2 within fractures in the host rock as has been suggested to occur due to the functioning of deeply rooted plants (e.g. Breecker et al., 2012b). Within the Blue Spring models, the effects of this additional CO_2 source do not appear to be substantial, but the role of such deep inputs has been suggested in other cave systems (e.g. Bergel et al., 2017) and is well suited to the spatially discretized domain of the RTM. This effect is explored by creating a supply of CO_2 introduced as a constant flux to the gas phase in the intermediate depth of 5–7 m below the upper boundary condition. The supply is radiocarbon modern and assigned a $\delta^{13}C$ value of -21%, typical of a vegetation signature. The effects are moderately apparent in the corresponding dissolved Ca^{2+} concentration (Fig. S7A),

where an uptick in dissolution rate of the limestone is evident at this intermediate depth and the final concentrations of Ca²⁺ reaching the cave as drip water are all uniformly elevated relative to the base case scenario (Fig. 9A). The corresponding pCO₂ is clearly affected (Fig. S7B), and all values increase as a result of this additional supply at 5 m depth. The effect on the radiocarbon DIC is perhaps the most unique (Fig. S7C) where the low pCO₂ soil boundary condition runs are clearly shifted towards much more negative values despite the fact that this CO₂ source is modern. This is directly related to the uptick in Ca²⁺ concentration noted above, which indicates the solubilization of more limestone. The extraordinarily low Δ^{14} C of this solid phase has a strong influence on the Δ^{14} C of DIC, thus overwhelming the effects of the modern pCO₂ source. Finally, the δ^{13} C value of DIC values are not very strongly influenced at all (Fig. S7D), as the new CO₂ source has a signature comparable to the surface boundary condition and the limestone does not exert such an extreme effect as in the case of radiocarbon. In total, this mass balance check indicates that out of the tracers considered here, the radiocarbon of DIC will be the most strongly impacted by a modern input of CO₂ at depth, but in a manner that may appear counterintuitive and is most influential when soil pCO₂ is low.

7. CONCLUSIONS

We report a novel application of isotope-enabled RTM software guided by a multi-year monitoring study to quantify the transport and transformation controls that dictate fluid solute chemistry and carbon isotope signatures in a karst environment. Measurements of cave air δ^{13} C indicate that the air is a mixture of surface air (higher δ^{13} C values) and air that seeps in from the soil zone through the host rock (lower δ^{13} C values), but a consistently modern Δ^{14} C implies the lack of a significant deep source of old organic matter contributing to cave air CO2. Drip rates and response to rainfall, as well as stable isotope signatures $(\delta^2 H, \delta^{18} O, \delta^{13} C)$, suggest Blue Spring hosts a variety of flow paths that are both quick to respond to surface signals (fracture-fed drips) and sites that are slower to respond and characterized by more water mixing and storage (diffuse-fed drips). Development of a forward, multicomponent reactive transport simulation that encapsulates the balance between reactivity of water draining through soil, flow rate, fluid saturation, gas diffusion and water-rock interaction immediately highlights a balance between generation of Ca concentrations as a result of limestone dissolution and associated maintenance of sufficiently modern DIC radiocarbon. This interplay offers a clear and tangible constraint on the behavior of a given cave system and the extent to which communication with the overlying atmospheric boundary couples to the solubilization of radiocarbon dead limestone. Following establishment of this balance, comparison between drip water δ^{13} C signatures and model results suggest that the most negative values may reflect fast flow rates and rapid transmission of signals through the host rock along fractures. Likewise, the least negative δ^{13} C values likely reflect some amount of degassing of CO₂ once the water emerges from the host rock onto the cave ceiling. These responses are muted in diffuse flow drip sites

Our reactive transport model suggests that fluids in the Blue Spring system do not reach saturation with respect to calcite. Further, forced degassing of fluid draining through the karst to promote the precipitation of carbonate within the host rock leads to sustained undersaturation with respect to the limestone, thus drawing the radiocarbon DIC values far too low relative to observations. In total, this mass balance assessment does not provide evidence for extensive prior calcite precipitation above the cave, but rather suggests that the higher δ^{13} C values of some drip waters are likely a result of degassing of CO2 in the open air of the cave ceiling. Indeed, when cave air pCO₂ values are pinned to a specific concentration at the lower boundary condition, as in the case of rapid communication between the cave entrance and interior, exchange between the fluid entering the cave ceiling and the cave air can even promote enhanced degassing and enrichment of δ^{13} C DIC.

In total this model development and calibration to the Blue Spring system highlight the necessity of the fluid draining through the host rock to be accompanied by a high degree of gas phase connectivity with the soil zone. If this free air diffusivity is diminished, it becomes extraordinarily difficult to achieve the basic balance between sufficient Ca concentrations and appropriately modern $\Delta^{14}C$ of DIC. The necessity of unimpeded gas phase mixing across the host rock is thus essential for modeling this system. A comparable requirement is anticipated in many similar karst systems except in instances where communication between the soil and host rock is permanently or seasonally hampered by water logging.

This reactive transport simulation offers a new linkage between the communication of cave air with the surrounding environment, the drainage rate of fluid into the subsurface and ultimately the chemical composition of fluids that form speleothems. Through this forward and predictive framework, we offer a new basis to consider the records karst Critical Zones offer in their ability to integrate fast responses to environmental and climate change (fast flow rates and surface connectivity) into the geologic timescales of speleothem records. Through the novelty and interdisciplinary nature of this work, we hope to provide a platform for hypothesis testing and a means of merging the relatively rapid rates of transformation characteristic of karst land-scapes into the broader study of Critical Zone structure and function.

Declaration of Competing Interest

The authors declare that they have no known competing financial interests or personal relationships that could have appeared to influence the work reported in this paper.

ACKNOWLEDGEMENTS

This work was supported grants from the National Science Foundation (EAR-1600931 to JLD and EAR-1600766 to JLO) and the Cave Research Foundation.

We thank Lonnie Carr for access to Blue Spring Cave and support of the research and Hal Love for guidance in the original field work. We also acknowledge countless field assistants from Vanderbilt University as well as Jaressa Hawkins, Ella Halbert, Nancy Hoang, and Cecily Shi (JENC), and Angela Eeds of the School for Science and Math at Vanderbilt. We thank two anonymous reviewers and David Richards and Daniel Breecker for valuable comments on this manuscript as well as Associate Editor Frank McDermott for handling the manuscript. Any use of trade, firm, or product names is for descriptive purposes only and does not imply endorsement by the U.S. Government.

DATA AVAILABILITY

Cave monitoring data are available as supplemental tables to this and the companion paper (Oster et al., this volume). Data are archived primarily through the USGS Sciencebase (https://doi:10.5066/P90OTSDY) and also in the Cave Monitoring Database (https://cave-monitoring.org). CrunchTope input files are available as supplementary information and the software is open source.

APPENDIX A. SUPPLEMENTARY MATERIAL

Supplementary data to this article can be found online at https://doi.org/10.1016/j.gca.2021.06.041.

REFERENCES

- Baker A., Ito E., Smart P. L. and McEwan R. F. (1997) Elevated and variable values of ¹³C in speleothems in a British cave system. *Chem. Geol.* **136**(3–4), 263–270.
- Banner J. L., Guilfoyle A., James E. W., Stern L. A. and Musgrove M. (2007) Seasonal variations in modern speleothem calcite growth in central Texas, USA. J. Sediment. Res. 77(8), 615–622.
- Bergel S. J., Carlson P. E., Larson T. E., Wood C. T., Johnson K. R., Banner J. L. and Breecker D. O. (2017) Constraining the subsoil carbon source to cave-air CO₂ and speleothem calcite in central Texas. *Geochim. Cosmochim. Acta* 217, 112–127.
- Breecker D. O., McFadden L. D., Sharp Z. D., Martinez M. and Litvak M. E. (2012a) Deep autotrophic soil respiration in shrubland and woodland ecosystems in Central New Mexico. *Ecosystems* **15**, 83–96.
- Breecker D. O., Payne A. E., Quade J., Banner J. L., Ball C. E., Meyer K. W. and Cowan B. D. (2012b) The sources and sinks of CO₂ in caves under mixed woodland and grassland vegetation. *Geochim. Cosmochim. Acta* **96**, 230–246.
- Breecker D. O. (2017) Atmospheric pCO₂ control on speleothem stable carbon isotope compositions. *Earth Planet. Sci. Lett.* **458**, 58–68.
- Carlson P. E., Banner J. L., Johnson K. R., Casteel R. C. and Breecker D. O. (2019) Carbon cycling of subsurface organic matter recorded in speleothem ¹⁴C records: Maximizing bombpeak model fidelity. *Geochim. Cosmochim. Acta* 246, 436–449.
- Cerling T. E., Solomon D. K., Quade J. A. Y. and Bowman J. R. (1991) On the isotopic composition of carbon in soil carbon dioxide. *Geochim. Cosmochim. Acta* 55(11), 3403–3405.
- Cerling T. E. (1984) The stable isotopic composition of modern soil carbonate and its relationship to climate. *Earth Planet. Sci. Lett.* **71**(2), 229–240.

- Covington M. D. (2016) 8. The importance of advection for CO₂ dynamics in the karst critical zone: An approach from dimensional analysis. Geol. Soc. Am. Special Pap. 516, 113–127.
- Dorale J. A., Edwards R. L., Ito E. and Gonzalez L. A. (1998) Climate and vegetation history of the midcontinent from 75 to 25 ka: a speleothem record from Crevice Cave, Missouri, USA. *Science* **282**(5395), 1871–1874.
- Dreybrodt W. and Scholz D. (2011) Climatic dependence of stable carbon and oxygen isotope signals recorded in speleothems: From soil water to speleothem calcite. *Geochim. Cosmochim. Acta* **75**(3), 734–752.
- Driese S. G., Srinivasan K., Mora C. I. and Stapor F. W. (1994) Paleoweathering of Mississippian Monteagle Limestone preceding development of a lower Chesterian transgressive systems tract and sequence boundary, middle Tennessee and northern Alabama. Geol. Soc. Am. Bull. 107(8), 998–1001.
- Druhan J. L., Guillon S., Lincker M. and Arora B. (2020a) Stable and radioactive carbon isotope partitioning in soils and saturated systems: a reactive transport modeling benchmark study. Comput. Geosci., 1–11.
- , Vol. 85Druhan, J. and Tournassat, C. (eds.) (2020b)Reactive Transport in Natural and Engineered Systems. Walter de Gruyter GmbH & Co KG.
- Druhan J. L. and Winnick M. J. (2019) Reactive transport of stable isotopes. *Elem.: Int. Mag. Mineral. Geochem. Petrol.* 15(2), 107–110.
- Druhan J. L., Winnick M. J. and Thullner M. (2019) Stable isotope fractionation by transport and transformation. *Rev. Mineral. Geochem.* 85(1), 239–264.
- Druhan J. L., Steefel C. I., Williams K. H. and DePaolo D. J. (2013) Calcium isotope fractionation in groundwater: molecular scale processes influencing field scale behavior. *Geochim. Cosmochim. Acta* 119, 93–116.
- Ersek V., Clark P. U., Mix A. C., Cheng H. and Edwards R. L. (2012) Holocene winter climate variability in mid-latitude western North America. *Nat. Commun.* **3**(1), 1–8.
- Fairchild I. J. and Baker A. (2012) Speleothem Science: From Process to Past Environments, Vol. 3. John Wiley & Sons.
- Fohlmeister J., Scholz D., Kromer B. and Mangini A. (2011) Modelling carbon isotopes of carbonates in cave drip water. *Geochim. Cosmochim. Acta* **75**(18), 5219–5228.
- Fohlmeister J. and Lechleitner F. A. (2019) STAlagmite dating by radiocarbon (star): A software tool for reliable and fast age depth modelling. *Quat. Geochronol.* **51**, 120–129.
- Fohlmeister J., Voarinstsoa N. R. G., Lechleitner F. A., Boyd M., Brandstätter M. J., Jacobson M. J. and Oster J. L. (2020) Main controls on the stable carbon isotope composition of speleothems. *Geochim. Cosmochim. Acta*, 10.1016/j. gca.2020.03.042 (in press).
- Frappier A. B., Sahagian D., Carpenter S. J., González L. A. and Frappier B. R. (2007) Stalagmite stable isotope record of recent tropical cyclone events. *Geology* **35**(2), 111–114.
- Frisia S., Fairchild I. J., Fohlmeister J., Miorandi R., Spötl C. and Borsato A. (2011) Carbon mass-balance modelling and carbon isotope exchange processes in dynamic caves. *Geochim. Cos-mochim. Acta* 75(2), 380–400.
- Genty D., Blamart D., Ghaleb B., Plagnes V., Causse C., Bakalowicz M., Zouari K., Chkir N., Hellstrom J., Wainer K. and Bourges F. (2006) Timing and dynamics of the last deglaciation from European and North African δ¹³C stalagmite profiles—comparison with Chinese and South Hemisphere stalagmites. *Quat. Sci. Rev.* **25**(17–18), 2118–2142.
- Genty D., Blamart D., Ouahdi R., Gilmour M., Baker A., Jouzel J. and Van-Exter S. (2003) Precise dating of Dansgaard-Oeschger climate oscillations in western Europe from stalagmite data. *Nature* **421**(6925), 833–837.

- Genty D., Baker A., Massault M., Proctor C., Gilmour M., Pons-Branchu E. and Hamelin B. (2001) Dead carbon in stalagmites: carbonate bedrock paleodissolution vs. ageing of soil organic matter. Implications for ¹³C variations in speleothems. *Geochim. Cosmochim. Acta* 65(20), 3443–3457.
- Genty D. and Massault M. (1999) Carbon transfer dynamics from bomb-¹⁴C and δ¹³C time series of a laminated stalagmite from SW France—modelling and comparison with other stalagmite records. *Geochim. Cosmochim. Acta* 63(10), 1537–1548.
- Genty D., Vokal B., Obelic B. and Massault M. (1998) Bomb ¹⁴C time history recorded in two modern stalagmites—importance for soil organic matter dynamics and bomb ¹⁴C distribution over continents. *Earth Planet. Sci. Lett.* **160**(3–4), 795–809
- Griffiths M. L., Fohlmeister J., Drysdale R. N., Hua Q., Johnson K. R., Hellstrom J. C., Gagan M. K. and Zhao J. X. (2012)
 Hydrological control of the dead carbon fraction in a Holocene tropical speleothem. *Quat. Geochronol.* 14, 81–93.
- Hendy C. H. (1971) The isotopic geochemistry of speleothems—I. The calculation of the effects of different modes of formation on the isotopic composition of speleothems and their applicability as palaeoclimatic indicators. *Geochimica et cosmochimica Acta* 35(8), 801–824.
- Jabro Jay D., Sainju Upendra M., Stevens William B. and Evans Robert G. (2012) Estimation of CO₂ diffusion coefficient at 0– 10 cm depth in undisturbed and tilled soils.. *Arch. Agron. Soil Sci.* 58(1), 1–9.
- Knierim K. J., Pollock E. D., Hays P. D. and Khojasteh J. (2015) Using stable isotopes of carbon to investigate the seasonal variation of carbon transfer in a Northwestern Arkansas Cave. *J. Cave Karst Stud.* 77(1).
- Lasaga A. C. (1981) Rate laws of chemical reactions: Rev.. Reviews in Mineralogy 8, 1–68.
- Lawrence C., Harden J. and Maher K. (2014) Modeling the influence of organic acids on soil weathering. *Geochim. Cosmochim. Acta* 139, 487–507.
- Lechleitner F. A., Fohlmeister J., McIntyre C., Baldini L. M., Jamieson R. A., Hercman H., Gasiorowski M., Pawlak J., Stefaniak K., Socha P. and Eglinton T. I. (2016) A novel approach for construction of radiocarbon-based chronologies for speleothems. *Quat. Geochronol.* 35, 54–66.
- Li L., Maher K., Navarre-Sitchler A., Druhan J., Meile C., Lawrence C., Moore J., Perdrial J., Sullivan P., Thompson A. and Jin L. (2017) Expanding the role of reactive transport models in critical zone processes. *Earth Sci. Rev.* 165, 280–301.
- Lichtner P. C. (1985) Continuum model for simultaneous chemical reactions and mass transport in hydrothermal systems. *Geochimica et Cosmochimica Acta* **49**(3), 779–800.
- Maher K. and Mayer K. U. (2019) Tracking diverse minerals, hungry organisms, and dangerous contaminants using reactive transport models. *Elem.: Int. Mag. Mineral. Geochem. Petrol.* 15(2), 81–86.
- Maher K., Steefel C. I., DePaolo D. J. and Viani B. E. (2006) The mineral dissolution rate conundrum: Insights from reactive transport modeling of U isotopes and pore fluid chemistry in marine sediments. *Geochim. Cosmochim. Acta* 70(2), 337–363.
- Maher K., DePaolo D. J. and Lin J. C. F. (2004) Rates of silicate dissolution in deep-sea sediment: In situ measurement using ²³⁴U/²³⁸U of pore fluids. *Geochim. Cosmochim. Acta* **68**(22), 4629–4648.
- Mattey D. P., Atkinson T. C., Barker J. A., Fisher R., Latin J. P., Durrell R. and Ainsworth M. (2016) Carbon dioxide, ground air and carbon cycling in Gibraltar karst. *Geochim. Cosmochim. Acta* **184**, 88–113.
- Matthews L. E. and Walter B. (2010) *Blue Spring Cave*. National Speleological Society, 340 p.

- Mickler P. J., Banner J. L., Stern L., Asmerom Y., Edwards R. L. and Ito E. (2004) Stable isotope variations in modern tropical speleothems: evaluating equilibrium vs. kinetic isotope effects. *Geochim. Cosmochim. Acta* 68(21), 4381–4393.
- Miorandi R., Borsato A., Frisia S., Fairchild I. J. and Richter D. K. (2010) Epikarst hydrology and implications for stalagmite capture of climate changes at Grotta di Ernesto (NE Italy): results from long-term monitoring. *Hydrol. Process.* 24(21), 3101–3114.
- Mook W. G. (2000) Environmental isotopes in the hydrological cycle. *Principles and Applications, IHP-V, Technical Documents in Hydrology* 1.
- Mook W. G. (1986) ¹³C in atmospheric CO₂. *Neth. J. Sea Res.* **20** (2–3), 211–223.
- Mook W. G., Bommerson J. C. and Staverman W. H. (1974) Carbon isotope fractionation between dissolved bicarbonate and gaseous carbon dioxide. *Earth Planet. Sci. Lett.* 22(2), 169– 176.
- Morel F. M. and Hering J. G. (1993) Principles and Applications of Aquatic Chemistry. *John Wiley & Sons*.
- Navarre-Sitchler A., Brantley S. L. and Rother G. (2015) How porosity increases during incipient weathering of crystalline silicate rocks. Rev. Mineral. Geochem. 80(1), 331–354.
- Noronha A. L., Johnson K. R., Southon J. R., Hu C., Ruan J. and McCabe-Glynn S. (2015) Radiocarbon evidence for decomposition of aged organic matter in the vadose zone as the main source of speleothem carbon. *Quat. Sci. Rev.* 127, 37–47.
- Noronha A. L., Johnson K. R., Hu C., Ruan J., Southon J. R. and Ferguson J. E. (2014) Assessing influences on speleothem dead carbon variability over the Holocene: implications for speleothem-based radiocarbon calibration. *Earth Planet. Sci. Lett.* 394, 20–29.
- Oster J. L., Covey A. K., Lawrence C., Giannetta M. G. and Druhan J. L. (this issue) A reactive transport approach to modeling cave seepage water chemistry II: Elemental signatures. *GCA Companion* (this issue).
- Oster J. L., Sharp W. D., Covey A. K., Gibson J., Rogers B. and Mix H. (2017) Climate response to the 8.2 kyr event in Coastal California. *Sci. Rep.* **7**, 3886.
- Oster J. L., Montanez I. P., Santare L. R., Sharp W. D., Wong C. and Cooper K. M. (2015) Stalagmite records of hydroclimate in central California during termination 1. *Quat. Sci. Rev.* 127, 199–214.
- Oster J. L., Montañez I. P. and Kelley N. P. (2012) Response of a modern cave system to large seasonal precipitation variability. *Geochim. Cosmochim. Acta* 91, 92–108.
- Oster J. L., Montanez I. P., Guilderson T. P., Sharp W. D. and Banner J. L. (2010) Modeling speleothem δ¹³C variability in a central Sierra Nevada cave using ¹⁴C and 87Sr/86Sr. *Geochim. Cosmochim. Acta* **74**(18), 5228–5242.
- Oster J. L., Montañez I. P., Sharp W. D. and Cooper K. M. (2009) Late Pleistocene droughts during deglaciation and Arctic warming. *Earth Planet. Sci. Lett.* **288**, 434–443.
- Polyak V. J., Asmerom Y., Burns S. J. and Lachniet M. S. (2012) Climatic backdrop to the terminal Pleistocene extinction of North American mammals. *Geology* 40(11), 1023–1026.
- Quade J., Cerling T. E. and Bowman J. R. (1989) Systematic variations in the carbon and oxygen isotopic composition of pedogenic carbonate along elevation transects in the southern Great Basin, United States. Geol. Soc. Am. Bull. 101(4), 464– 475.
- Rudzka D., McDermott F., Baldini L. M., Fleitmann D., Moreno A. and Stoll H. (2011) The coupled δ¹³C-radiocarbon system-

- atics of three Late Glacial/early Holocene speleothems; insights into soil and cave processes at climatic transitions. *Geochim. Cosmochim. Acta* **75**(15), 4321–4339.
- Rudzka-Phillips D., McDermott F., Jackson A. and Fleitmann D. (2013) Inverse modelling of the ¹⁴C bomb pulse in stalagmites to constrain the dynamics of soil carbon cycling at selected European cave sites. *Geochim. Cosmochim. Acta* 112, 32–51.
- Steefel C. I., Appelo C. A. J., Arora B., Jacques D., Kalbacher T., Kolditz O., Lagneau V., Lichtner P. C., Mayer K. U., Meeussen J. C. L. and Molins S. (2015) Reactive transport codes for subsurface environmental simulation. *Comput. Geosci.* 19(3), 445–478.
- Steefel C. I. and Maher K. (2009) Fluid-rock interaction: A reactive transport approach. *Rev. Mineral. Geochem.* **70**(1), 485–532.
- Stuiver M. and Polach H. A. (1977) Discussion reporting of 14 C data. *Radiocarbon* **19**(3), 355–363.
- Swoboda-Colberg N. G. and Drever J. I. (1993) Mineral dissolution rates in plot-scale field and laboratory experiments. *Chem. Geol.* **105**(1–3), 51–69.
- Tremaine D. M. and Froelich P. N. (2013) Speleothem trace element signatures: A hydrologic geochemical study of modern cave dripwaters and farmed calcite. *Geochim. Cosmochim. Acta* 121, 522–545.
- Trumbore S. (2009) Radiocarbon and soil carbon dynamics. *Annu. Rev. Earth Planet. Sci.* **37**, 47–66.
- Trumbore S. E. (1993) Comparison of carbon dynamics in tropical and temperate soils using radiocarbon measurements. *Global Biogeochem. Cycles* **7**(2), 275–290.
- Velbel M. A. (1993) Constancy of silicate-mineral weathering-rate ratios between natural and experimental weathering: implications for hydrologic control of differences in absolute rates. *Chem. Geol.* **105**(1–3), 89–99.
- White, A.F. and Buss, H.L., 2014. 7.4-Natural weathering rates of silicate minerals. Treatise on Geochemistry, Second Edition. Elsevier, Oxford, pp.115-155.
- Willmott C. J., Rowe C. M. and Mintz Y. (1985) Climatology of the terrestrial seasonal water cycle. *J. Climatol.* **5**(6), 589–606.
- Wolery, T.J. and Daveler, S.A., 1992. EQ6, a computer program for reaction path modeling of aqueous geochemical systems: Theoretical manual, users guide, and related documentation (Version 7.0); Part 4 (No. UCRL-MA-110662-Pt. 4). Lawrence Livermore National Lab., CA (United States).
- Wang Y., Amundson R. and Trumbore S. (1993) Processes controlling the ¹⁴C content of soil carbon dioxide: Model development. *Chem. Geol.* **107**(3–4), 225–226.
- Wong C. I. and Breecker D. O. (2015) Advancements in the use of speleothems as climate archives. *Quat. Sci. Rev.* **127**, 1–18.
- Wong C. I., Banner J. L. and Musgrove M. (2015) Holocene climate variability in Texas, USA: An integration of existing paleoclimate data and modeling with a new, high-resolution speleothem record. *Quat. Sci. Rev.* 127, 155–173.
- Wong C. and Banner J. L. (2010) Response of cave air CO₂ and drip water to brush clearing in central Texas: Implications for recharge and soil CO₂ dynamics. *J. Geophys. Res. Biogeosci.* **115**(G4).
- Zhang J., Quay P. D. and Wilbur D. O. (1995) Carbon isotope fractionation during gas-water exchange and dissolution of CO₂. Geochim. Cosmochim. Acta 59(1), 107–114.

Associate editor: F. McDermott